RUHR-UNIVERSITÄT BOCHUM

RUB

RUHR-UNIVERSITÄT BOCHUM

Ab initio calculations for the reaction mechanisms of polycyclic aromatic hydrocarbons with O(^{3}P)

Özlem Yönder

Masters Thesis – September 22, 2017.
International Masters Program Molecular Sciences with a Focus on Spectroscopy and Simulation (iMOS).

Supervisor: Prof. Dr. Christof Hättig

iMOS

Abstract

Oxy-fuel technology is a promising modification to the operations of conventional coal power plants in order to reduce their air pollution and green-house gas emissions. Combustion of coal occurs in two steps: Pyrolysis and char burn-out. Here, we start to build a char combustion kinetic model from quantum chemical tools. We have chosen a set of linear and branched polycyclic aromatic hydrocarbons (PAHs) as the representative building blocks of char. In particular, we studied the reactions of PAHs with O-atoms ($O(^3P)$) on the triplet surface, using the TPSSh density functional, the Grimme D3 correction, and the TZVP basis set. Accordingly, the topology and size of the PAHs were shown to have an effect on the O-atom addition reaction due to the rearrangement of orbitals. Additionally, for the O-atom addition and subsequent hydrogen abstraction reactions, the activation barriers were shown to correlate linearly with the reaction energies.

Erklärung

Hiermit versichere ich, dass ich die vorliegende Arbeit selbstständig verfasst und keine anderen als die angegebenen Quellen und Hilfsmittel benutzt habe, dass alle Stellen der Arbeit, die wörtlich oder sinngemäß aus anderen Quellen übernommen wurden, als solche kenntlich gemacht sind und dass die Arbeit in gleicher oder ähnlicher Form noch keiner Prüfungsbehörde vorgelegt wurde.

DATE	AUTHOR

Contents

1 Introduction **1**

1.1 Motivation 1

1.2 Model Selection 2

1.3 Reaction Mechanisms 6

1.4 Objective of the Thesis 8

1.5 Organization of the Thesis 10

2 Background and Methods **11**

2.1 Model Structures and Aromaticity 11

2.1.1 Topology 11

2.1.2 Aromaticity 13

2.1.3 Classification 15

2.2 Reaction Path Optimization 15

2.3 Methods 17

3 Results and Discussion **19**

3.1 O Atom Addition and H Radical Abstraction 19

3.1.1 Reaction Path of Benzene 19

3.1.2 Oxygen Addition: Reaction Energies 21

3.1.2.1 Linear Polycyclic Aromatic Hydrocarbons 26

3.1.2.2 Angularly Fused (Branched) Polycyclic Aromatic Hydrocarbons 27

3.1.3 Oxygen Addition: Activation Barriers 29

3.1.4 Hydrogen Abstraction: Reaction Energies 33

3.1.5 Hydrogen Abstraction: Activation Barriers 33

3.2 OH Abstraction 35

4 Conclusions and Summary **40**

5 Outlook **42**

6 Acknowledgment **44**

List of Figures **45**

List of Tables **47**

Bibliography **48**

A Appendix **54**

A.1 Sample Stabilization Energy Calculation 54

A.2 Energies of the Optimized Structures 55

A.2.1 Oxygen Addition and Hydrogen Abstraction Reaction 55

A.2.2 OH Abstraction Reaction 60

1 Introduction

1.1 Motivation

For a sustainable economy, immediate steps towards clean energy production should be taken. A strategy may be to 1) achieve higher energy efficiency, 2) reduce CO_2 emissions, and 3) shift fuel use to clean energy sources. Coal-fired power plants produce about 40% of global electricity. Therefore, a promising intermediate solution can be the integration of conventional coal power plants with oxy-fuel combustion technology to decrease air pollution and greenhouse gas emissions.

As an oxidizer, oxy-fuel combustion technology uses a mixture of O_2, and recycled flue gas, which is mainly CO_2, instead of the conventional oxidizer air. Oxygen can be supplied by a cryogenic air separation process.[6] One of the advantages of oxy-fuel technology is its suitability for carbon capture and storage (CCS). Another advantage is the lower NO_x emission intensities as compared with that of air-coal combustion. The reasons are, respectively, the lower N_2 partial pressure and higher CO_2 concentration in oxy-fuel combustion, and the partially recycled NO_x which is reburned during combustion.[6] On the other hand, the kinetics of char oxidation do not show a significant difference between air and oxy-fuel combustion conditions according to the thermogravimetric measurements.[46, 47, 30] Slight differences in the rate are attributed to the observation that char-CO_2 reaction rates are three to four orders of magnitude smaller than char-O_2 reactions.[46] One of the concerns about oxy-fuel combustion technology is the SO_2 accumulating in the furnace because of the recycled flue gas. Even though the sulfur conversion does not change significantly under oxy-fuel and air combustion, the accumulation of SO_x in oxy-fuel technology increases potential corrosion problems at the end of the flue gas duct.[43]

In order to consider all of these aspects, computational fluid dynamics (CFD) modeling is a comprehensive tool, because CFD can be used to study fluid flow, heat transfer and chemical reactions. However, currently CFD simulations use very simplified reaction mechanisms for coal combustion. For example, a kinetic model for the combustion and gasification of char follows the reactions:[29]

$$\mathrm{C_{(s)}} + \mathrm{O_2} \longrightarrow \mathrm{CO_2} \tag{1.1}$$

$$\mathrm{C_{(s)}} + 1/2\,\mathrm{O_2} \longrightarrow \mathrm{CO} \tag{1.2}$$

$$\mathrm{C_{(s)}} + \mathrm{CO_2} \longrightarrow 2\,\mathrm{CO} \tag{1.3}$$

$$\mathrm{C_{(s)}} + \mathrm{H_2O} \longrightarrow \mathrm{CO} + \mathrm{H_2} \tag{1.4}$$

$$\mathrm{C_{(s)}} + 2\mathrm{H_2} \longrightarrow \mathrm{CH_4}. \tag{1.5}$$

Even though such a simplification is useful because of the high computational cost of the detailed combustion models in CFD simulations, with the increasing computing power and development of the computational models, the use of detailed models may become feasible in the near future. Nevertheless, a detailed kinetic model of char combustion still does not exist. Additionally, the existing models use the parameters obtained from fits to experimental data, and therefore, it is unclear how they correspond to the microscopic rate constants. As a result, these models fail to predict the reaction rates when the char composition is outside the composition range of the char samples used to build the empirical kinetic model. Therefore, we aim to build a detailed reaction mechanism of char combustion using a bottom-up approach from first principles calculations as a part of the SFB/TRR 129 Oxyflame project. This project aims to develop a multi-scale model for oxyfuel combustion that reaches from the microscopic level up to the level of furnaces in actual power plants.

1.2 Model Selection

Oxidation of coal is affected by internal factors, such as composition, physical properties, and particle size, as well as by external factors, such as temperature, partial pressure of O_2, and moisture content in the medium.[48] A basic illustration for

the fundamental processes during the combustion of coal is shown in Figure 1.1. In terms of the internal factors, the composition and structure of coal influences the oxidation kinetics. Therefore, there have been a vast amount of models for the structure of coal. The review article of Mathews and Chaffee [32] represents a historical evolution of coal structural models for brown, subbituminous, bituminous, and anthracite coal. One of the early influential coal models was proposed by Given in

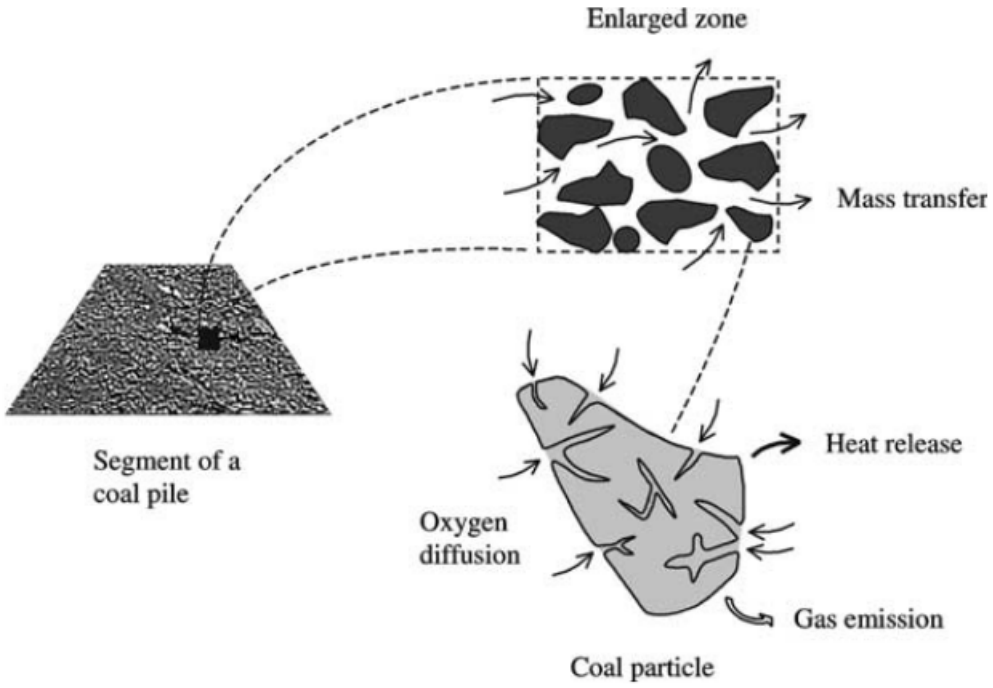


Figure 1.1: Simplified illustration of oxidation of coal. Taken from Wang et al.[48]

1959 for bituminous coal[16]. The model was based on X-ray diffraction and infrared spectroscopic studies indicating 75% of the carbons in aromatic systems, absence of long alkyl chains, and, paradoxically, attachment of 80% of the hydrogens to the carbon atoms which are not in the aromatic system. Therefore, they proposed small aromatic systems, 1-3 fused rings, linked by highly substituted aliphatic groups as shown in Figure 1.2.

In general, apart from C and H, coal structural models may include the presence of N in the form of amide, amine, hydrooxylamine, or indole; S in the form of thiol, thiophene, or thioether; inorganic ions such as those originating from Na, Ca, and

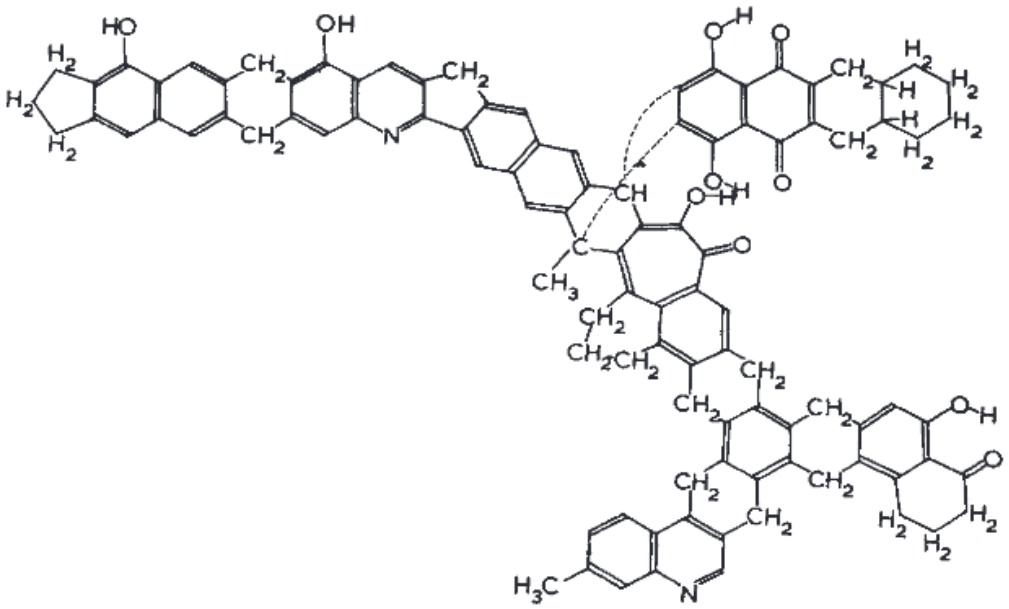


Figure 1.2: A bituminous coal model from 1959 with formula $C_{102}H_{78}O_{10}N_2$ evidenced from the distribution of hydrogen based on the X-ray diffraction and infra-red spectroscopic studies. Taken from Given.[16]

Mg; transition metals such as Fe and Ni; as well as oxygen containing functional groups such as carboxylic acid, phenols, aryl-O cross-links, aliphatic ether, keto and alcohol groups, and furan analogues.[32] Some of these models also consider the effect of H-bonding and π-π stacking.[32] By the development of computational tools in 1990s, the first 3D coal structural models were also studied using force fields or ab-initio methods.[32]

The combustion of coal starts by pyrolysis reactions, which involve bond breaking, vaporization, condensation, and cross-linking. Then, the residual char reacts. Because the pyrolysis is faster than char burn-out, the latter can be considered as the rate limiting process.[39] That is, the volume of the combustion chamber is mainly affected by the burning rate of the char.[39] Additionally, even though char reactivity depends on the actual fuel, it is believed that the reactivity is less dependent to the fuel as compared with the pyrolysis step. For that reason, we plan to start by building a char combustion model instead of a coal combustion model, so that it excludes the pyrolysis process.

The Raman spectroscopy is a fast and non-destructive tool for characterization of carbon materials. Raman spectra of these materials has two main bands: G and D bands. The first lies at around 1560 cm^{-1} (G peak) and results from the bond stretching of sp^2 carbon atoms. The latter lies at around 1360 cm^{-1} (D peak) and is a result of breathing modes.[12, 13] According to the number of layers, the G and the second order D peak (2D peak) change in shape, position, and relative intensity.[12, 13] Furthermore, the intensity ratio of the D and G peaks provides information about the disorder of the material.[12, 13] Several studies used Raman spectroscopy to characterize char to understand the amorphous content and the structural features of the ordered structures. For example, a recent study assigned the bands observed in Raman spectroscopic analysis of five series of chars, produced from avicel cellulose at final heating temperatures between 400 to 700 ℃.[40] They calculated spectra of naphtalene, pyrene, perylene, benzo[a]pyrene, benzo[ghi]perylene, and coronene using density functional theory (DFT). Accordingly, they concluded that char involves cycloheptane and larger ring systems, small PAHs at the size scale of naphthalene to pyrene as well as large ring systems greater than coronene. They could not assign the source of the amorphous bands around 1400-1460 cm^{-1}; however, they assigned the bands between 1480 cm^{-1} and 1550 cm^{-1} to the coupling of symmetric breathing modes and asymmetric stretching modes. This coupling orgininates from the restriction of asymmetric stretches due to the point defects and heteroatom (such as oxygen) defects of these amorphous structures.[40]

Other studies focused on the effect of the heating rate and temperature of pyrolysis, and the inorganic content on the structure of char. Lu, Kong, Sahajwalla, and Harris [31] studied the change of char structure during pyrolysis and combustion by quantitative X-Ray diffraction analysis (QXRDA) and high-resolution transmission electron microscopy (HRTEM). They prepared the char from a low volatile bituminous coal from Central Queensland in Australia using a 99% v/v N_2 and 1% v/v O_2 gas mixture at four different heating rates. As a result, they observed that char becomes more ordered as the temperature increases or the heating rate decreases; therefore, it becomes less reactive.[31] Specifically, during pyrolysis the amorphous concentration decreases and aromatic concentration increases.[31] Another study on char structure under various heat treatment conditions was performed using Raman spectroscopy by Sheng.[38] This study showed that the content of inorganic matter

on the structure of char, independent of coal type and heat treatment conditions, is minor; however, it affects the char reactivity.

Because the higher amorphous content of char is associated with increased reactivity, we start by studying combustion of the aromatic rings in char. Additionally, we exclude the effect of inorganic matter. Therefore, we start by studying combustion reactions of a set of polycyclic aromatic hydrocarbons as a model system.

1.3 Reaction Mechanisms

To the best of our knowledge, the experimental investigations of the products of char combustion measure typically only the CO, CO_2, NO_x, and SO_x composition in the product stream. On the other hand, reactive force field simulations have been used to identify the reaction mechanisms on the model char structures. For example, a ReaxFF reactive force field study at the temperatures 3000-4000 K on a coal char model, built as a distribution of aromatic structures, has shown that the char oxidation is initialized by either thermal degradation or by oxygen molecules and O and OH radicals.[5] They also observed that the 6-membered rings are transformed into 5- and 7-membered rings which then subsequently decomposed into smaller fragments.[5] Another ReaxFF simulation has been conducted at the temperature range of 2000-4000 K to investigate the pyrolysis and char burn-out of a brown coal model. As a result, they observed that during the combustion, apart from H_2O and CO_2, gases such as C_2H_4, CH_4, CH_3, and HCHO are also released.[3]

From a more simplified perspective, combustion reactions of benzene can be expected to be in many respects prototypical for the combustion mechanisms of larger aromatic rings. According to the reaction network built by Brezinsky, during the initial steps of the oxidation of benzene, a radical pool of H, OH, O, and HO_2 is formed.[11, 4] Then, these radicals react with benzene to form phenyl radicals, phenols, phenoxy radicals, cyclopentadienyl radicals, cyclopentadienolyl radicals, and followed by the ring opening butadienyl radicals and butadienes.[11, 4] Similar products were also observed in a recent study in 2010 performed using a multiplexed chemical kinetics photo-ionization mass spectrometer.[42] Accordingly, the products of the benzene and oxygen atom reaction includes phenol and phenoxy radicals

together with cyclopentadiene and cyclopentadienyl radicals.[42] Based on the reaction network of Brezinski et al.[4], Emdee et al.[11] built an adiabatic, constant pressure, homogeneous kinetic model and compared the results with the flow reactor experiments. They attributed the differences to the exclusion of the turbulence in the kinetic model, which accelerates the reaction. According to their reaction path analysis, the main combustion routes are through the reactions

$$C_6H_6 + OH \longrightarrow C_6H_5 + H_2O \tag{1.6}$$

$$C_6H_6 + O \longrightarrow C_6H_5O + H \tag{1.7}$$

and that phenol is produced from the reaction

$$C_6H_5O + H \longrightarrow C_6H_5OH \tag{1.8}$$

which is then primarily consumed by the reaction

$$C_6H_6OH + OH \longrightarrow C_6H_5O + H_2O. \tag{1.9}$$

The importance of the reaction 1.7 has been supported by the quantum chemical studies of the reaction of benzene with $O(^3P)$.[42, 33] The experimentally determined activation barrier for the benzene oxygen reactions is around 4.5 kcal/mol [34, 27], which is close to the calculated barrier of 4.9 kcal/mol for the oxygen atom addition to the benzene ring according to the CBS-QB3 calculations by Nguyen [33] and 5.7 kcal/mol at the G3B3' level of theory by Taatjes [42]. Therefore, it is believed that this reaction is the rate controlling step. Additionally, for the intermediate structure formed upon oxygen atom addition, an intersystem crossing (ISC) to the singlet state is possible through a conical intersection between two spin states.[42, 33]

Nguyen et al.[33] concluded that the dissociation of the product of the reaction 1.7 back to the reactants predominates above 1500 K whereas ISC dominates below 800 K. same conclusion was evidenced in the study of Taatjes et al.[42] comparing the ratio of the products from gas phase reactions; showing as the dominant products phenol and phenoxy+H at or below 500 K, and phenoxy+H and cyclopentadiene+CO above 700 K (Figure 1.3).

On the triplet surface, the hydrogen abstraction reaction from the intermediate structure formed upon oxygen atom addition to benzene (reaction 3 in Figure 1.3)

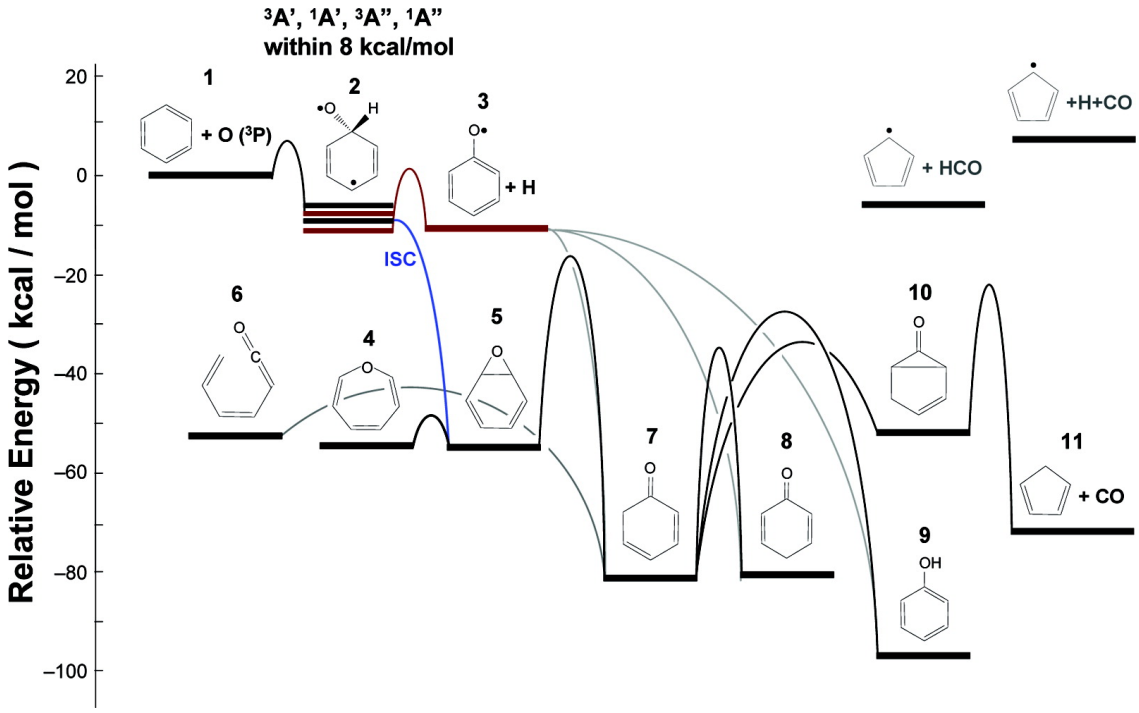


Figure 1.3: Reaction paths of O-atom addition reaction to benzene. Taken from Taatjes et al.[42]

has an activation barrier of 14.5 kcal/mol calculated at the CBS-QB3 level [33] and 11.4 kcal/mol at the G3B3' level[42]. Taatjes pointed out that this high activation barrier does not agree with the experimental activation brrier of 4.5 kcal/mol. Therefore, this reaction is assumed to be unimportant on the triplet energy surface [42]. Another reaction on the triplet surface could be the abstraction of an H-atom by formation of OH radical. According to the calculations of Nguyen, the activation barrier of this step is 11.6 kcal/mol,[33] which similarly does not agree with the experimental results for the activation barrier.

1.4 Objective of the Thesis

Here, we investigate the reaction mechanisms of a set of polycyclic aromatic hydrocarbons (PAHs) with an oxygen atom ($O(^3P)$). The set of PAHs are determined such that there is a variety of different sizes and molecular regions (such as armchair edge or bay region, fjord region, and zigzag edge) of PAHs. We have studied the reactions

only on the triplet energy surface. The three reactions studied are analogous to the following reactions of benzene: i) O-atom addition reaction

$$C_6H_6 + O(^3P) \rightarrow \cdot C_6H_6O \cdot \tag{1.10}$$

followed by ii) the H abstraction step

$$\cdot\, C_6H_6O \cdot \rightarrow \cdot C_6H_5O + H \cdot \tag{1.11}$$

and iii) the direct H abstraction with formation of OH radical

$$C_6H_6 \rightarrow \cdot C_6H_5 + \cdot OH. \tag{1.12}$$

Reaction 1.10 is the reaction which is considered to be the most important reaction on the triplet surface for benzene [42, 33], whereas the reactions 1.11 and 1.12 were considered to be unimportant[42] for the combustion of benzene because of higher activation barriers than the experimentally obtained ones. However, the different topology or electronic structure of PAHs might result in lower activation barriers. For that reason, here, the analogous reactions for a set of selected PAHs for these two reactions 1.11 and 1.12 on the triplet surface together with the O-atom addition reaction 1.10 are studied. In other words, this thesis investigates the reaction pathways and transition states for the reactions analogous to 1.10, 1.11 and 1.12 on the C-H bonding carbon sites of a set of PAHs with different molecular regions and sizes. Analysis of the results will provide information about the main factors that determine the differences in the reactivities. If the variations in reactivity with the size and shape of PAHs as well as the most reactive sites within a certain kind of PAH can be understood, it will allow for the selection of a set of prototypical PAH sites and the extra-/intrapolation of the reaction rates for other sites of other PAHs from the results of this set.

Additionally, through these calculations, the work protocol has been tested. That is, the suitability of first finding all of the stationary points with TPSS functional and SVP basis set, and second, re-optimizing the structures using the hybrid TPSSh functional, TZVP basis set, and Grimme D3 dispersion correction has been tested.

1.5 Organization of the Thesis

In Section 2 the selected PAHs, the reaction path optimization method, and the procedure we have used in the calculation of the reaction paths are explained. The results are represented together with the discussions in Section 3. It is divided mainly in two parts. The first part explains the findings based on the density functional theory (DFT) calculations for the O-atom addition and H abstraction reactions. Especially for the O-atom addition step, the effect of angularity and size on the reactivity have been discussed. The second part represents the preliminary results for the OH radical abstraction reaction. Then, Section 4 concludes the findings. Section 5 explains the next steps we plan to take to build the coke combustion model. In Section A, the reader can find a sample calculation of the stabilization energy, and the total energies and zero point energies of the structures used for the calculation of the reaction energies and activation barriers.

2 Background and Methods

This section provides background information about the polycyclic aromatic hydrocarbons considered and their aromaticity. Additionally, the chain-of-states method that we have used for the transition state search is also explained.

2.1 Model Structures and Aromaticity

2.1.1 Topology

We have chosen a set of linear and branched polycylic aromatic hydrocarbons (PAHs). The set is chosen such that there are PAHs with different levels of angularity and a variety of sizes. For the linear PAHs a set from benzene to pentacene has been considered. Among single row PAHs, phenanthrene and anthracene are isoelectronic. Similarly, tetracene, benz[a]anthracene, chrysene, benzo[c]phenanthrene, and triphenylene are isoelectronic with different level of angularities. We have also considered PAHs which are not single row. Among them anthanthrene and benzo[ghi]perylen are isoelectronic. The sites are considered for the C-H bonding carbon atoms of the PAHs. Only the positions that are not related by symmetry are considered. Each site is numbered as in Figure 2.1.

The molecular regions of polyarenes are sometimes classified as K-,L-, or M-regions (Figure 2.2) based on the quantum mechanical theories of carcinogenesis developed by Pullman [36]. The K-region possess more double bond character than the other bonds in an aromatic ring system; therefore, it is considered to be more reactive, and hence, of interest in carcinogenic studies. L region is a mesomolecular region.[19] It is shown that K- and M- regions are activating carginogenetic

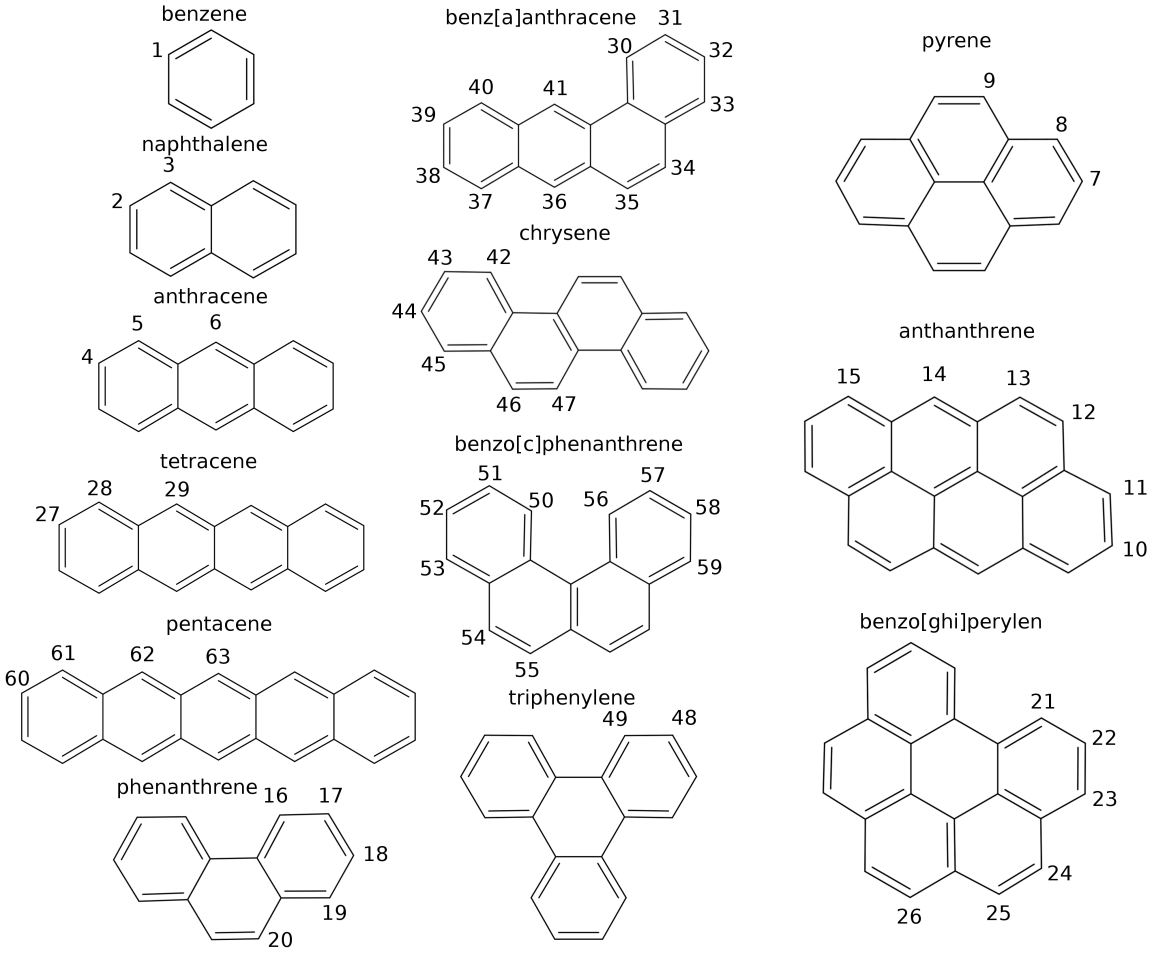


Figure 2.1: The sites for the linear and branched PAHs considered.

effect whereas L- region has a deactivating effect.[45] On the other hand, the naming of the bay and fjord regions originates from NMR studies, and refers to the sterically crowded molecular regions. These regions show downfield shifts in NMR spectroscopy, which are more pronounced for the fjord regions the bay regions.[19] The bay region is sometimes also called "backdoor of K- region."[19]

Among the molecules considered here, all but benzo[c]phenanthrene have planar ground state structures. Benzo[c]phenanthrene has a hellical structure in its ground state. Therefore, even though it is symmetric, the attack of oxygen from inside or outside of the helical structure is symmetrically different. Hence, we have calculated the reaction energies of benzo[c]phenanthrene for both case near the fjord region.

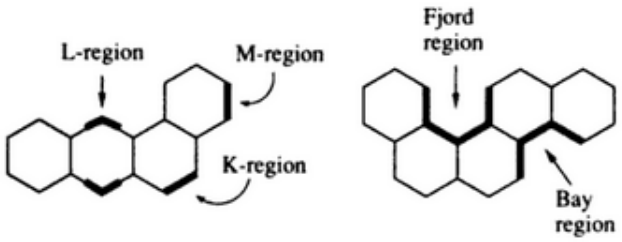


Figure 2.2: Molecular regions of polyarenes. Taken from Harvey. [19]

2.1.2 Aromaticity

In order to get an overall perspective for the aromaticity of the PAHs, we have calculated the harmonic oscillator model of aromaticity (HOMA)[28] for each individual six membered ring. HOMA is a geometry based aromaticity criteria using C-C bond lengths that use that of benzene as a reference. It is defined by,

$$\mathrm{HOMA} = 1 - \frac{\alpha}{n}\sum_{i=1}^{n}(r_{CC} - r_{CC-benzene})^2 \tag{2.1}$$

where n is the number of CC bonds in the ring and α is an empricial constant with a value 257.7 $Å^{-2}$, so that HOMA=0 for the Kekulé structure of benzene, and HOMA=1 for the aromatic form of benzene. That is, a deviation from HOMA=1 shows the degree of deviation from the aromatic character of the benzene.

Figure 2.3 shows the HOMA values calculated using the geometries of the PAHs optimized by TPSSh functional, TZVP basis set, and Grimme D3 dispersion correction. Accordingly, some features of the aromaticity of the PAHs considered are as follows:

- Upon linear fusion of a six membered ring (i.e. going from benzene (a) to pentacene (e)) the aromatic character decreases. (It is worth noting that Hückel Molecular Orbital (HMO) Theory predicts the reverse trend, because according to the HMO Theory the resonance energy per atom increases with the size of acenes.)
- Within each linearly fused PAH the innermost ring is the most aromatic one.

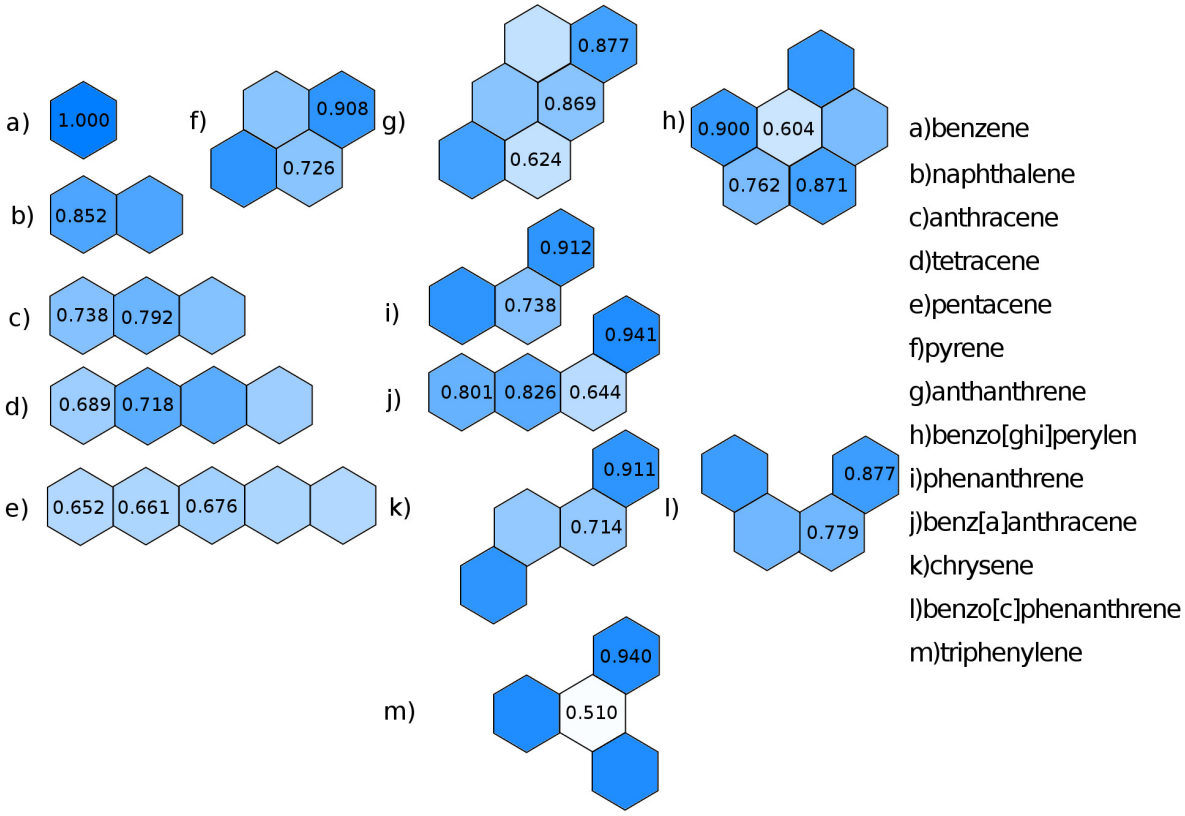


Figure 2.3: Some selected linear and branced polycyclic aromatic hydrocarbons and their HOMA values.

- Comparing anthracene (c) with phenanthrene (i), we see that an angular fusion causes an increase in the aromaticity of the outer ring, whereas the middle ring becomes less aromatic.
- Similarly, comparing the angularly fused end of benz[a]anthracene (j) with tetracene (d) we see the same pattern. However, the linear tail shows an acene-like character with the outermost ring being less aromatic (HOMA=0.801) than the neighbouring one in the L-region (HOMA=0.826).
- The difference in HOMA on the angular tail is 0.43 for triphenylene (m), 0.30 for benz[a]anthracene (j), 0.20 for chrysene (k), and 0.10 for benzo[c]phenanthrene (l).
- The rings of pyrene (f) have a similar aromaticity as phenanthrene (i).

2.1.3 Classification

Taking into account the topological and aromatic character of the PAHs, we have classified the molecules from naphtlane (a) to pentacene (e) and the linear tail of benz[a]anthracene as linearly fused, and all the others as angularly fused (branched).

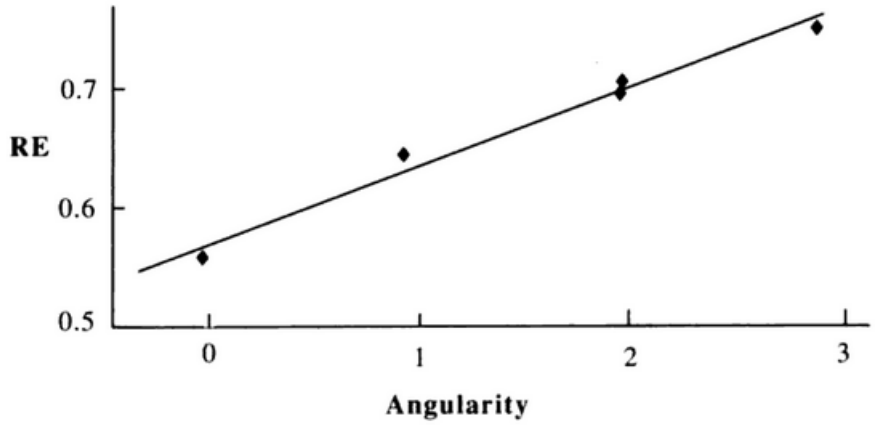


Figure 2.4: Correlation between resonance energy (RE) and angularity of the PAHs tetracene (0), benz[a]anthracene (1), chrysene (2), benzo[c]phenanthrene (2) and triphenylene (3). Taken from Harvey. [20]

The angularity of the PAHs have been discussed before by other scientists. For example, Zander has pointed out that the resonance energies of the ring systems have a linear correlation with angularity as shown in Figure 2.4.[52, 20] In relation with the reactivity, Clar has observed that the reactivity of PAHs for the Diels Alders reactions increases with linear fusion and decreases with angular fusion.[7, 20] Additionally, according to the studies on the Diels-Alders reactions, the most reactive ring is the middle ring for the linear PAHs, even though it is the most aromatic one as well [37].

2.2 Reaction Path Optimization

The transition state (TS) structures are the first-order saddle points on the potential energy surface. Therefore, unlike the minima, it is challenging to find them. Several methods to find them include nonlocal methods, such as nudged elastic band (NEB),

and local methods, such as Trust Region Image Minimization (TRIM). Nonlocal methods use typically the reactant and product geometries to approximately locate the TS structure. In other words, they do not locate the actual TS. Local ones, on the other hand, do not use reactant and product geometries. Instead, they require a good estimate of the TS structure to propagate the geometry using the gradient and usually at least an approximate Hessian of the current point.[26] Therefore, in searching for a transition state, first a nonlocal method is used to locate a point on the reaction pathway that is sufficiently close to the transition state. A point is close to the TS structure if the Hessian matrix at the point has only a single negative value and the corresponding eigenvector is parallel to the reaction pathway. Only after such a TS guess is found, can the local methods be used to converge to the first order saddle point. When the transition state is found, the reaction path can be located by following the intrinsic reaction coordinate[15].

The nonlocal methods may use one-structure or two or more structures to locate the saddle point. The simplest one-structure method is the linear synchronous transit (LST) method. This method generates an initial coordinate by assuming that all the internuclear distances from reactants to products vary linearly through an interpolation of the internuclear distances.[18] The transition state estimate is then the highest energy structure. However, the coordinates generally do not change synchronously; therefore, the LST method rarely provides a good TS guess.[26] An improvement on the LST method can be made by assuming a parabolic reaction path and minimizing the energy in the direction perpendicular to the LST path.[26] This assumption is called the Quadratic Synchronous Transit (QST) method. The multiple structure interpolation methods (chain-of-state methods) are more commonly used. These methods not only approximate the TS but also the whole reaction path.[26] The initial distribution of the structures is generally generated by a LST path; however, if desired, intermediate geometries can be used to lead the reaction path guess in a certain direction.[26] The Nudged Elastic Band (NEB) belongs to this class of methods. It adds a spring interaction between adjacent images so that the path is continuous; that is, it creates an elastic band.[23] This band is then optimized together with the minimization of forces acting on the images.[23] Because of the different projection of the two force parts, the optimization methods for NEB becomes inefficient.[26] To address this problem, a modification to the NEB

method is to allow one of the images to climb up along the elastic band, which is therefore called the Climbing Image Nudged Elastic Band method (CI-NEB).[24] Another commonly used method is the String Method. This method samples the configurations using strings instead of points in the configuration space.[8] That is, it re-distributes the points after each optimization cycle.[26] Here, as a nonlocal method, we have used a chain-of-states method which approximates the potential energy surface as a quadratic function as implemented in TURBOMOLE under "woelfling" code.[1] In contrast to the Nudged Elastic Band or String Method, the only constraint in this reaction path optimization method is the equal spacing of the structures.[35]

The most common local methods are based on the augmented Hessian Newton-Raphson (NR) approach.[26] The NR step maximizes the energy along the Hessian TS eigenvector and minimizes along all the other directions. Here, we used the Trust Radius Image Minimization (TRIM) method. The TRIM method, as the other augmented Hessian NR methods to find the TS structure, increases the energy along the reaction direction and decreases it in all the other directions. On the other hand, the TRIM method generates the step by optimizing a single function instead of generating two different functions along the reaction coordinate and the transverse modes.[21] The NR methods for TS optimization require a good starting geometry and a Hessian. Therefore, as an alternative, the dimer method has been proposed. This method identifies the reaction direction using two displaced images.[22, 25]

2.3 Methods

As a preliminary structure search, the meta-GGA functional TPSS [44] and the SVP basis set were used. This was especially essential for the transition state search calculations; otherwise, the transition state structure search would have taken longer because using hybrid functionals, such as TPSSh functional, the computation of the exact exchange part is costly.

We have optimized the final geometries and calculated their zero point energies by density functional theory (DFT) using:

- the TPSSh hybrid exchange correlation functional with 10% exact exchange [41],
- the TZVP basis set, which includes three contracted gaussian type orbitals in the valence shell and adds one set of polarization function, and
- the Grimme-D3 correction,[17] which contains two and three body interaction corrections to the Kohn-Sham DFT energy,

as implemented in TURBOMOLE. The reason we have used the dispersion correction is that, for large molecules, dispersive interactions might be significant. For all of the calculations, the resolution of the identity approximation has been applied using auxiliary basis sets[10, 49].

All of the calculations are performed in TURBOMOLE. The energies are calculated using the module "ridft". The self-consistent field (SCF) convergency criterion was 10^{-6} Hartree. We have used multiple grid "m3", in which "m" stands for multiple, and the number represents a value between 1 (coarse and least accurate) and 5 (most dense). The zero point energies are calculated using the "aoforce" module. The geometry optimizations are performed using the program "statpt" with the option "itrvec 0" to find the minima on the potential energy surface and "itrvec 1" to find the first order saddle points. The transition state search was performed using the "woelfling" code.

3 Results and Discussion

3.1 Oxygen Atom Addition and Hydrogen Radical Abstraction Reactions for PAHs

This group of reactions can be formulated as

$$C_{2n}H_{n+a} + O(^3P) \longrightarrow \cdot C_{2n}H_{n+a}O\cdot \longrightarrow \cdot C_{2n}H_{n+a-1}O + H\cdot \qquad (3.1)$$

where $0 \leq a \leq 3$. Here, the polyaromatic hydrocarbon $C_{2n}H_{n+a}$ is referred as S1, the intermediate structure $\cdot C_{2n}H_{n+a}O\cdot$ as S2, and the product after hydrogen abstraction $\cdot C_{2n}H_{n+a-1}O$ as S3. Similarly, the transition states will be referred to as TS1 for the oxygen ($O(^3P)$) addition step, and TS2 for the hydrogen ($H\cdot$) abstraction step.

3.1.1 Reaction Path of Benzene

Here, only the reaction path for benzene is explained, because all the other PAHs studied follow a similar reaction path. Figure 3.1 shows the reaction path for benzene. When the reactants come closer, they pass through a van der Waals (vdW) structure before reaching the first transition state (TS1). The calculated activation barrier of this step is 1.8 kcal/mol if calculated from the van der Waals structure ($Ea_{1-vdW \longrightarrow TS1} = E_{TS1} - E_{vdW} = 1.8\,kcal/mol$), and -1.0 kcal/mol if calculated from the separate reactants $O(^3P)$ and benzene ($Ea_1 = E_{TS1} - E_{S1} - E_{O(^3P)} = -1\,kcal/mol$). (Even though the first calculation as $Ea_{1-vdW \longrightarrow TS1}$ is more intuitive–because by definition an activation barrier should be positive–the activation barriers of PAHs are reported using the second definition as Ea_1 within the

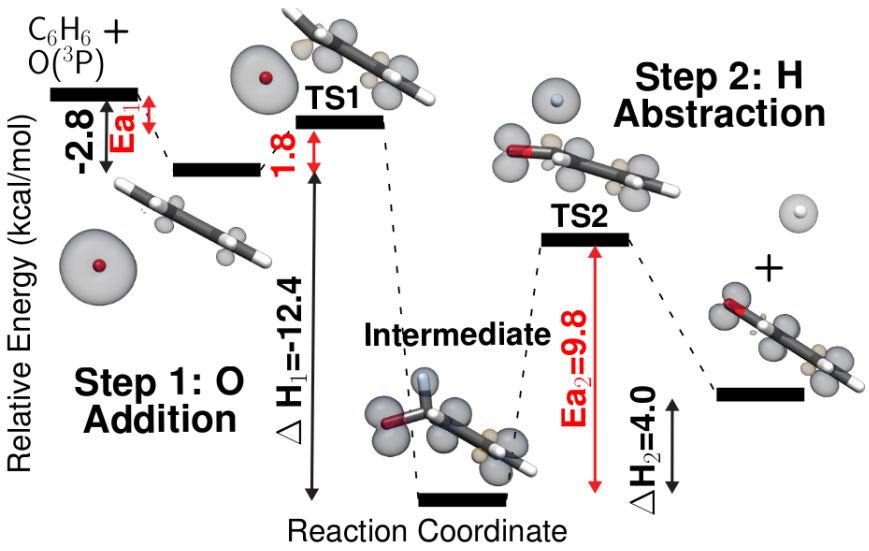
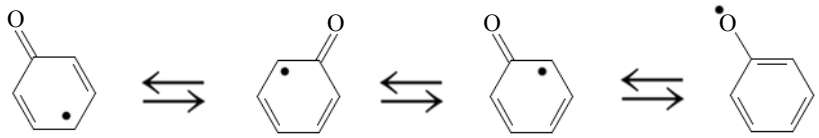


Figure 3.1: The reaction path of benzene for O(^{3}P) addition, following hydrogen radical abstraction reactions and showing spin densities.

thesis. Therefore, the reported activation barriers for the O-atom addition reaction have negative values.)

In the oxygen addition step, an electron from O(^{3}P) is transferred to the lowest unoccupied molecular orbital (LUMO) of benzene, resulting in an intermediate structure (S2). This electron is transferred to the ring system as shown in Figure 3.2 in the second column. The other electron of the O(^{3}P) stays on the oxygen. In the H abstraction step, the σ-CH bond of the benzene breaks, resulting in the final structure S3. In this structure, oxygen becomes conjugated with the ring system, as represented in the Lewis notation in Equation 3.2.



(3.2)

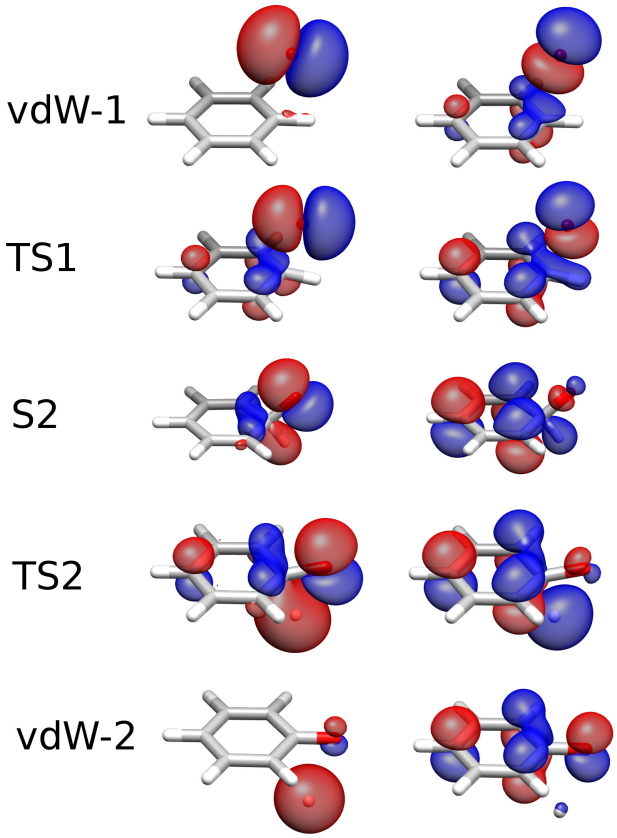


Figure 3.2: Singly occupied orbitals during the reaction of benzene with O(^{3}P).

3.1.2 Oxygen Addition: Reaction Energies

The exothermicity of the O addition reaction originates from the C-O σ bond formation between the O(^{3}P) atom and the ring system. On the other hand, by the addition of oxygen, the aromaticity of the ring system as well as the C-H bond are distorted, both of which require energy.

Even accounting for the C-H deformation, the out-of-plane angle between the C-H bond and the ring system is also important; the C-H bond length change is easier to measure. Therefore, only the C-H bond length changes upon O-atom addition have been analyzed. Table 3.3 shows the data for the C-H bond length change for each individual site. From the reactants to the intermediate S2 structure the C-H bond length increases by 3.7 pm on average with a standard deviation of 0.5 pm. Such a small change indicates that this effect is not the main contributor to the difference in the reaction energies.

Table 3.3: The change in the C-H bond length from the reactant S1 to the intermediate S2 and to the transition state TS1 in the units of pm.

ID	$\mathbf{\Delta d_{TS1}}$	$\mathbf{\Delta d_{S2}}$	22		4.0	44		3.9
1	0.1	3.8	23		3.9	45		3.8
2	-0.2	4.0	24		3.9	46		4.0
3		3.7	25		4.0	47		3.6
4	-0.2	4.0	26		3.9	48	-0.2	3.9
5		1.5	27		4.1	49		3.5
6		3.7	28		4.0	50		3.0
7	-0.2	1.6	29		3.9	51		3.9
8		3.8	30		3.6	52	-0.4	4.2
9		3.9	31		3.9	53		3.9
10		4.0	32	-0.2	3.9	54		4.1
11		3.9	33	-0.1	3.7	55		3.4
12	-0.3	4.1	34		4.0	56		1.8
13		3.7	35	-0.2	4.0	57		3.8
14		3.8	36		3.8	58	-0.4	3.4
15		4.0	37		3.9	59		3.6
16		3.9	38		3.9	60		4.2
17		3.6	39		3.9	61		4.1
18		3.9	40		3.9	62		4.0
19		3.8	41		3.2	63		3.9
20		4.0	42		3.6	$\mathbf{\bar{\Delta}d}$	-0.2	3.7
21		3.7	43	-0.3	3.9	$\boldsymbol{\sigma}$	0.1	0.5

In order to account for the effect of breaking the aromaticity of the ring system, we calculated the stabilization energies using the Hückel Molecular Orbital Theory (HMO). A sample calculation can be found in Appendix A.1. It is worth to note that the HMO theory accounts only for the contributions of the Hamilton matrix elements corresponding to the two nearest neighboring carbons to the total energy. Therefore, the interactions due to the hydrogens are not included when using the HMO theory.

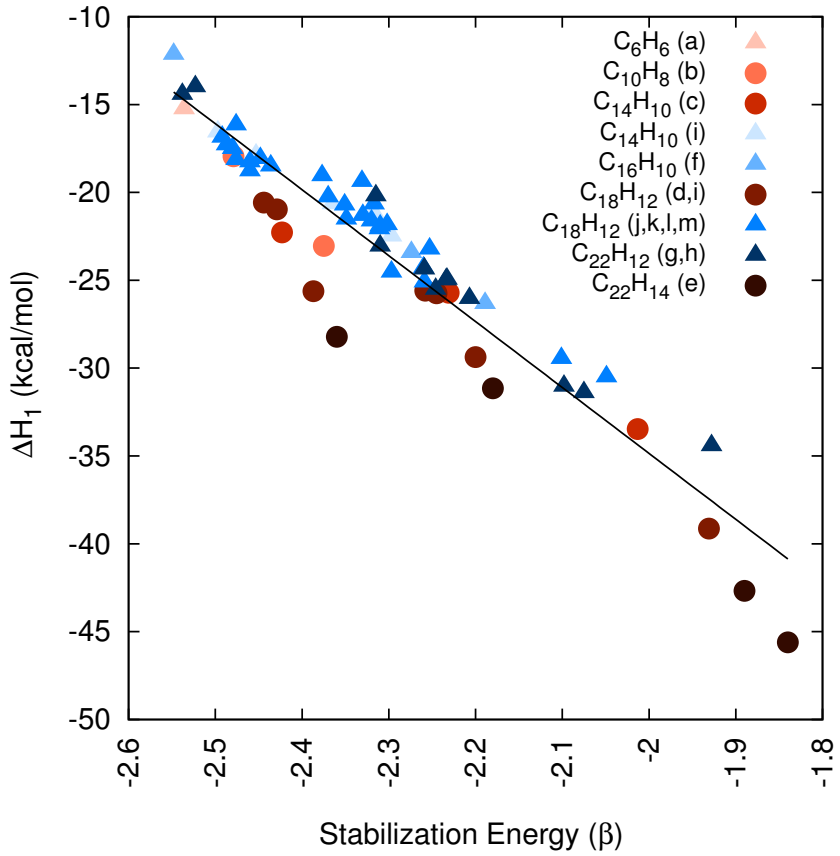


Figure 3.4: Enthalpy change of the oxygen addition reaction vs the stabilization energy classified according to the size of the molecules and fusion of the ring that the reaction proceeds. "●" represents linear fusion and "▲" represents angular fusion. The letters a-m represent the molecules given in Figure 2.3.

Accordingly, there is a linear relation between the stabilization energy, $E_{stabilization}$, that is calculated using the HMO Theory and the enthalpy of the oxygen addition reaction, ΔH_1, that is calculated using DFT/TPSSh-D3 (Figure 3.4). A linear fit gives the relation

$$\Delta H_1\,[\text{kcal/mol}] = -37.5\,[\text{kcal/mol}]\,E_{stabilization} \cdot \beta^{-1} - 109.9\,[\text{kcal/mol}] \qquad (3.3)$$

with a coefficient of determination (R^2) of 0.905. This implies that the differences in the reaction energies originates mainly from the rearrangements of the orbitals of the π-system. Figure 3.6 shows the SOMOs of the intermediate structure S2 for each individual site.

Table 3.5: The first column is the ID of the corresponding site, the second column is the stabilization energy, the third column is ΔH_1 calculated using DFT, the fourth column is ΔH_1 calculated from the stabilization energy fit given in Equation 3.3, and the last column is $\Delta = \Delta H_1 - \Delta H_1(\text{fit})$.

ID	β	ΔH_1	ΔH_1(fit)	Δ
1	-2.54	-15.2	-14.8	-0.4
2	-2.48	-17.9	-16.9	-1.0
3	-2.38	-23.1	-20.8	-2.2
4	-2.42	-22.3	-19.0	-3.2
5	-2.23	-25.7	-26.2	0.5
6	-2.01	-33.5	-34.4	0.9
7	-2.55	-12.1	-14.4	2.2
8	-2.19	-26.3	-27.8	1.5
9	-2.27	-23.4	-24.6	1.2
10	-2.23	-25.0	-26.1	1.1
11	-2.10	-31.0	-31.2	0.2
12	-2.54	-14.4	-14.7	0.3
13	-2.08	-31.4	-32.1	0.7
14	-1.93	-34.4	-37.6	3.2
15	-2.23	-24.9	-26.2	1.2
16	-2.45	-17.9	-17.9	0.0
17	-2.37	-20.7	-21.2	0.6
18	-2.50	-16.6	-16.3	-0.3
19	-2.32	-21.2	-23.0	1.8
20	-2.30	-22.5	-23.8	1.3
21	-2.25	-25.5	-25.7	0.2
22	-2.52	-14.0	-15.3	1.3
23	-2.21	-26.0	-27.1	1.1
24	-2.26	-24.4	-25.2	0.8
25	-2.31	-23.1	-23.3	0.2
26	-2.32	-20.2	-23.1	2.9
27	-2.39	-25.6	-20.4	-5.2
28	-2.20	-29.4	-27.4	-2.0
29	-1.93	-39.1	-37.5	-1.6
30	-2.37	-20.3	-21.0	0.8
31	-2.44	-18.5	-18.6	0.1
32	-2.49	-17.3	-16.6	-0.7
33	-2.32	-20.7	-23.0	2.4
34	-2.26	-25.1	-25.2	0.1
35	-2.26	-24.3	-25.2	0.9
36	-2.05	-30.5	-33.1	2.6
37	-2.25	-25.7	-25.7	0.0
38	-2.44	-20.6	-18.3	-2.3
39	-2.43	-21.0	-18.8	-2.1
40	-2.26	-25.6	-25.2	-0.4
41	-2.10	-29.4	-31.1	1.7
42	-2.35	-21.5	-21.8	0.3
43	-2.45	-18.1	-18.1	0.0
44	-2.49	-16.9	-16.5	-0.4
45	-2.30	-21.8	-23.6	1.7
46	-2.25	-23.2	-25.4	2.2
47	-2.35	-20.7	-21.7	1.0
48	-2.48	-16.2	-17.1	0.9
49	-2.38	-19.0	-20.8	1.7
50	-2.33	-19.4	-22.5	3.1
51	-2.46	-18.3	-17.7	-0.6
52	-2.48	-18.1	-17.1	-1.1
53	-2.31	-22.1	-23.2	1.2
54	-2.30	-24.5	-23.8	-0.8
55	-2.32	-21.6	-22.9	1.3
56	-2.33	-21.3	-22.5	1.2
57	-2.46	-18.8	-17.7	-1.1
58	-2.48	-17.5	-17.1	-0.4
59	-2.31	-21.9	-23.2	1.3
60	-2.36	-28.2	-21.3	-7.0
61	-2.18	-31.2	-28.0	-3.1
62	-1.89	-42.7	-38.9	-3.8
63	-1.84	-45.6	-40.8	-4.9

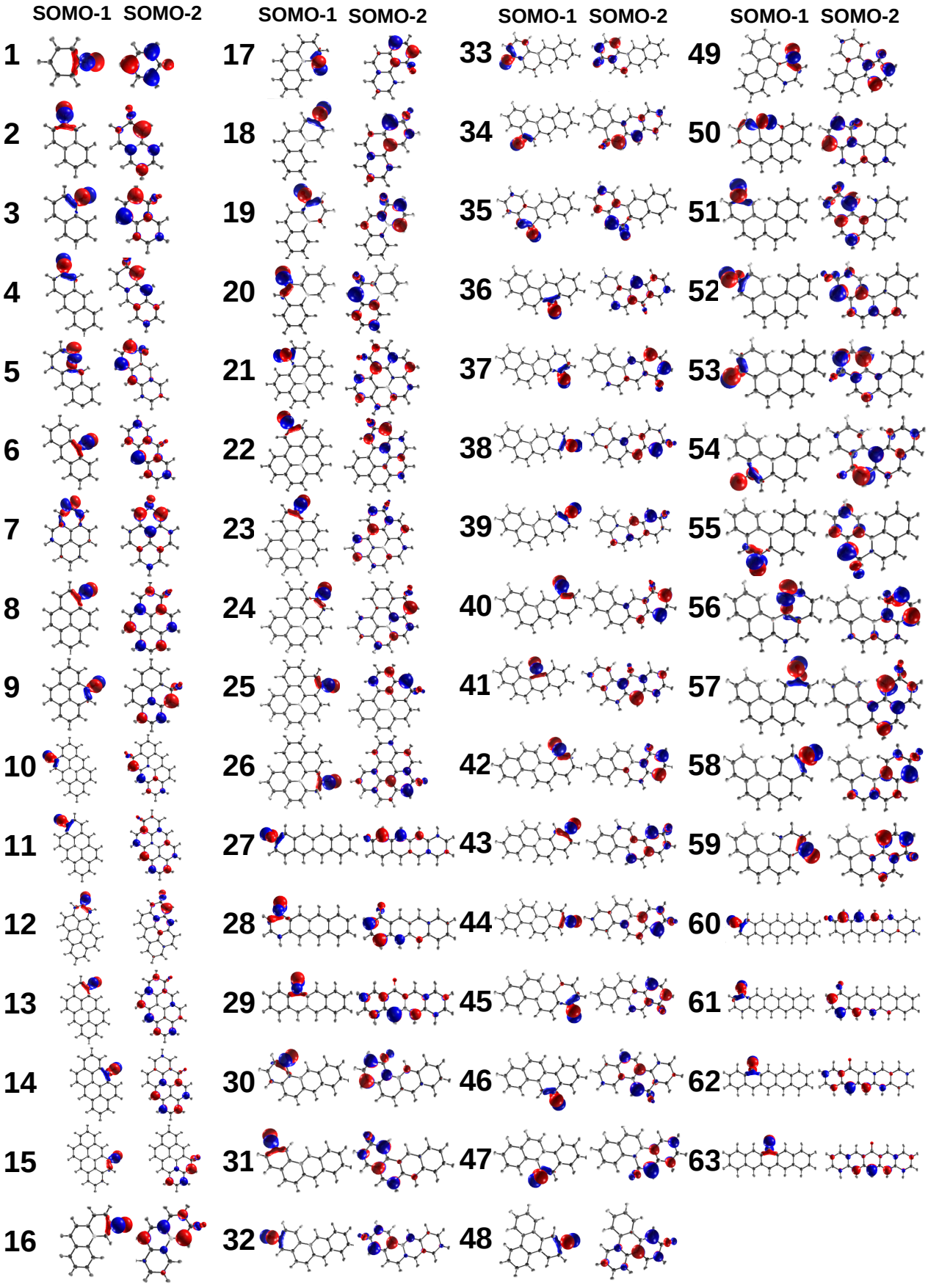


Figure 3.6: SOMOs of the PAHs studied for the structure S2.

3.1.2.1 Linear Polycyclic Aromatic Hydrocarbons

Figure 3.7 shows the reaction energies for different sites. For benzene all of the sites are equivalent. There are two different sites for naphthalene, three different sites for anthracene and tetracene, and four different sites for pentacene. We also considered the linear tail of benz[a]anthracene; it is closer to anthracene in reaction energies than tetracene.

The trends in the reaction energies of acenes (linear PAHs), as seen in Figure 3.7, indicates that as the size of the PAH increases, the O-atom addition reaction gets more exothermic. This observation can be explained by the fact that the unpaired electron on the ring system gets more delocalized as the size of the molecule increases, because the larger the acene becomes the smaller is the loss in stabilization (i.e. resonance) energy from S1 to S2. Additionally, Figure 3.7 shows that within each linear PAH, the site on the inner ring is the most exothermically reacting site. This is because the loss in the stabilization energy is smaller when the reaction occurs at a ring in the middle than when it occurs at an outer ring.

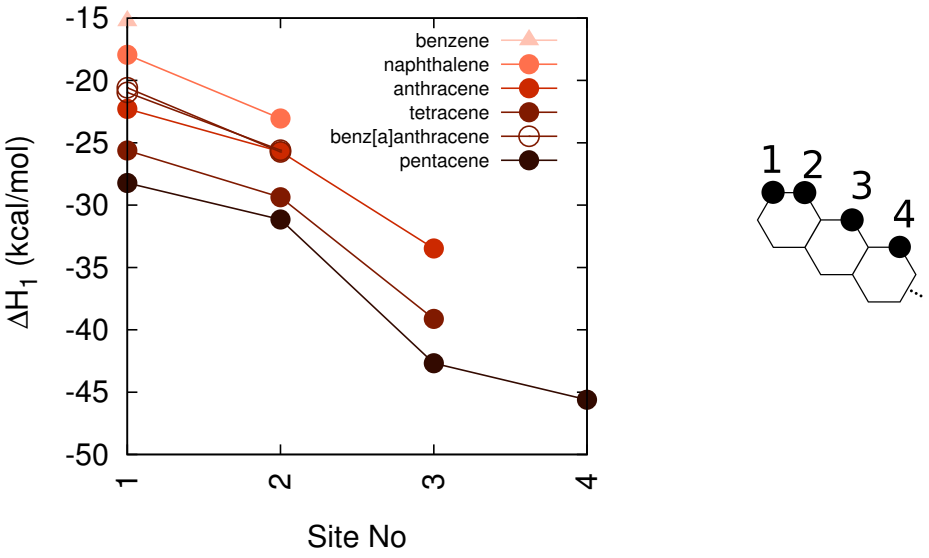


Figure 3.7: Comparison of the reaction energies for different sites of linear PAHs.

It has been known already that for the Diels-Alders reactions the reactivity of the linear PAHs increases with the increasing PAH size and that the central ring is the most reactive one.[37] The higher reactivity of the middle ring has also been

known in acene isomerization [9, 50]. Additionally, the difference in the reactivity of α and β carbon sites, which are respectively referred as 2 and 1 in Figure 3.7, was detected by mass spectroscopy of the products of naphthalene oxidation reaction with the O-atom to give a 7:1 mass ratio of α-naphthol and β-naphthol.[51]

3.1.2.2 Angularly Fused (Branched) Polycyclic Aromatic Hydrocarbons

Analogy to the linearly fused rings:

Figure 3.8 shows the reaction energies for the angularly fused sites. Within the single row branched PAHs we can compare the energies of the sites at the first angularly fused ring by making an analogy to the linearly fused sites as represented in Figure 3.9. Accordingly, we can say from Figure 3.8 and 3.10 that sites in the vicinity of the bay or fjord carbon atoms have a general trend for the reaction energy as Bay-2 > Bay-1 > Bay > Bay-3 and similarly Fjord-2 > Fjord-1 > Fjord > Fjord-3, with the same trend that we have seen from Figure 3.7 for the acenes and the linear tail of the benz[a]anthracene.

Sterically crowded bay and fjord regions:

Here we compare the reaction energies at the bay and fjord sites in order to understand the effect of the hydrogens making these regions sterically crowded.

The fit to the stabilization energy explains the differences in the reaction energies as the result of the orbital rearrangements. However, for the reactions at sites 50 and 56 of benzo[c]phenanthrene, the reaction energies differ even though the stabilization energies are the same. Benzo[c]phenanthrene is the only PAH which is not planar among the other PAHs considered. Instead, it is helical due to the hydrogens in the fjord region. Therefore, from which side the oxygen approaches makes a difference in the reaction energies. One can see from Figure 3.11-b that there is a stronger hydrogen interaction between the oxygen and hydrogen of the neighboring fjord region carbon when oxygen attacks from inside of helix. On the other hand, if it attacks from the back, the hydrogens of the neighboring fjord-carbons get closer which creates a repulsion. Thus, site 56 results in a more stable intermediate

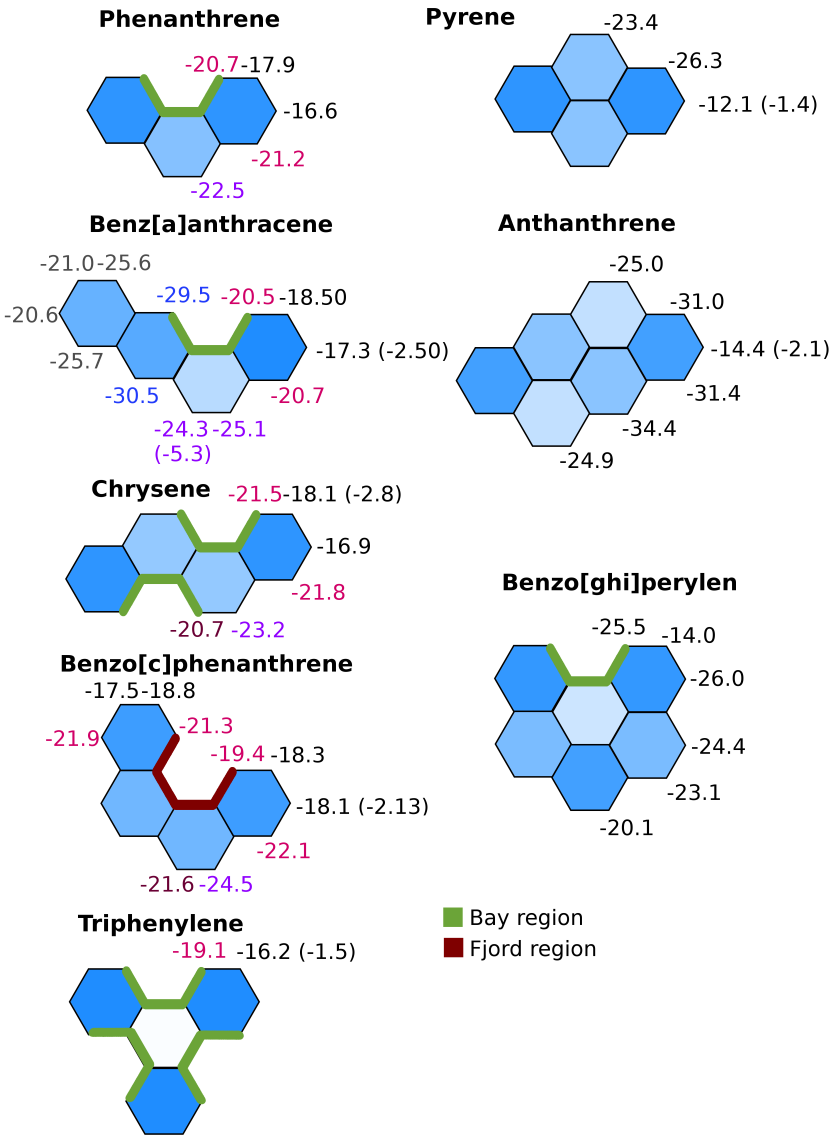


Figure 3.8: Reaction energies, ΔH_1, and the activation barriers, (Ea_1), for the angularly fused PAHs shown on the reactant PAHs colored according to their HOMA values.

structure. Therefore, site 56 is more reactive than site 50 (Figure 3.11).

When the reactions at the bay region of benz[a]anthracene are compared (Figure 3.12), we observe that the reaction at site 41 is 9.1 kcal/mol more exothermic. This is also estimated by the stabilization energy difference. The electron is more delocalized when O adds to site 41 than to site 30.

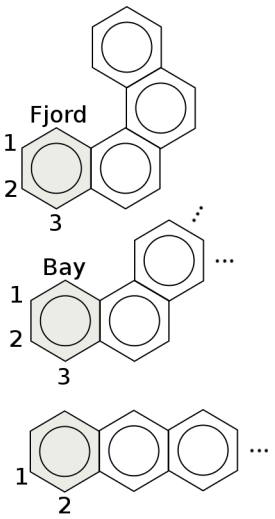


Figure 3.9: Classification of the quartet sites.

When one looks at the bay regions of chrysene from the spin density, one cannot see a significant difference. In fact, this is the reason why both of the sites have very similar reaction energies. However, when the bond lengths are compared it is observed that in site 42 the O—H bond distance is shorter than 47 and the H—H distance is longer. That is, the reason why site 42 is more exothermic than site 47 is because of the interaction of hydrogen and oxygen, even though their stabilization energy is the same from the HMO guess.

3.1.3 Oxygen Addition: Activation Barriers

For the kinetics of a reaction the activation energies are important. However, the calculation of the activation energies is computationally demanding because geometry optimization of a transition state requires a good starting geometry. On the other hand, calculation of reaction energies requires only the optimization of the reactants and products. In some cases, the reaction energies can even be estimated without any quantum mechanical calculations such as when using Benson's additivity rules [2]. Therefore, it is desirable to find a relationship between the activation barriers and reaction energies.

For the oxygen addition step, among the sites considered, only the sites 1, 2,

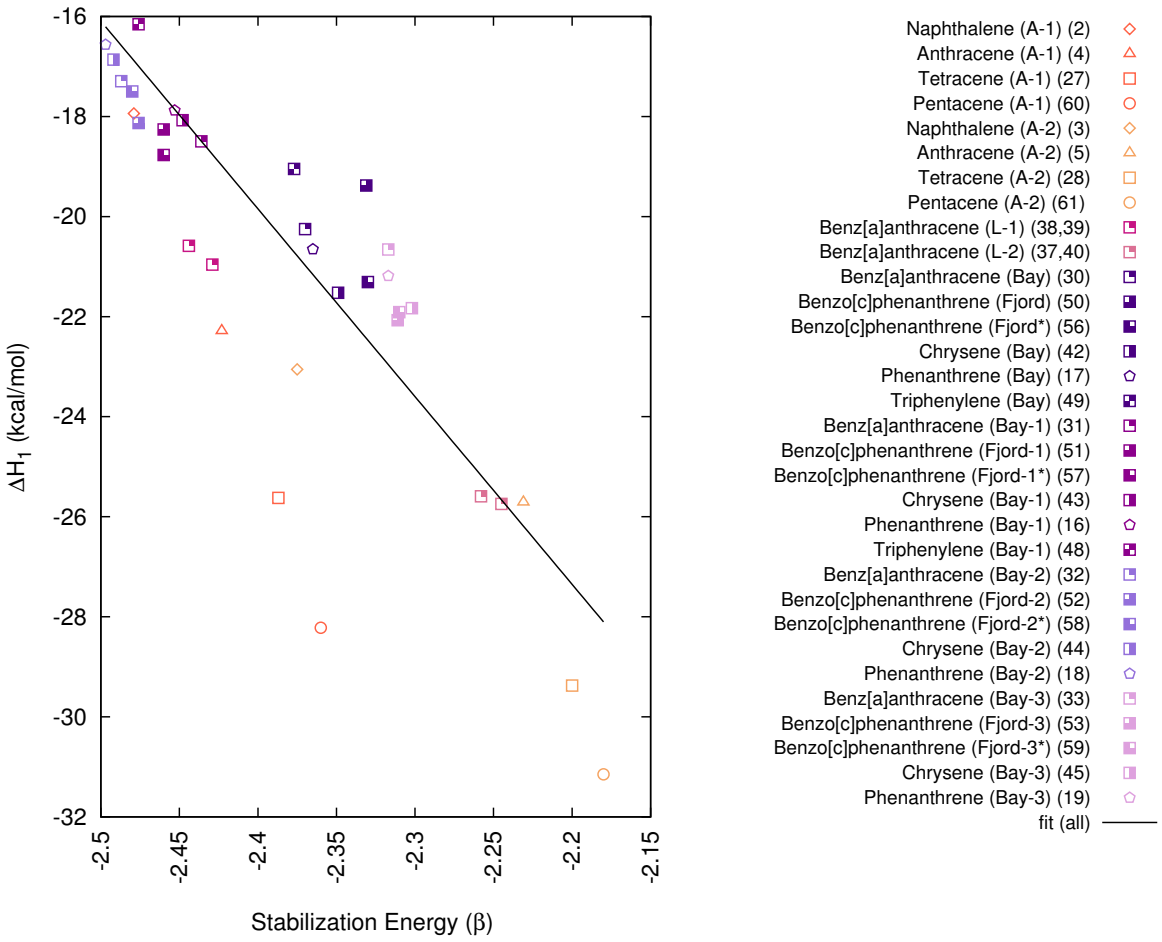
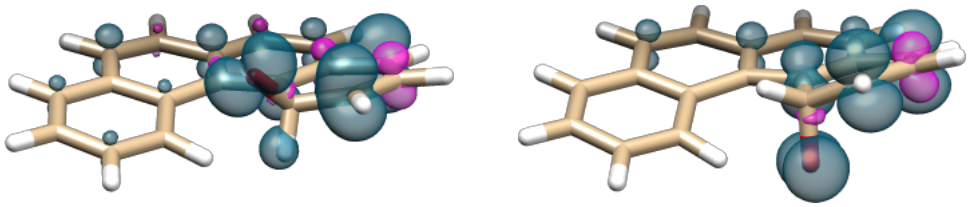


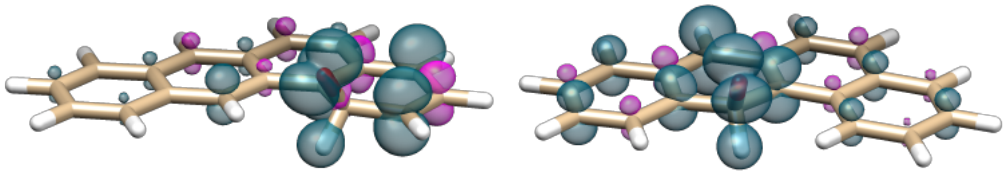
Figure 3.10: Reaction energy vs stabilization energy. In the labels A represents the sites on the acenes whereas L represents the sites on benz[a]anthracene which are on the linearly fused tail of the molecule. The numbers next to these notations denote the order of attachment as also represented in Figure 3.9. The other numbers given in paranthesis seperately are the IDs of different sites used within the report. Fjord* represents the site of the benzo[ghi]perylen to which the O atom attacks from the site where it comes close to the neighboring fjord H atom.

4, 7, 12, 16, 18, 19, 26, 30-33, 38, 39, 43-45, 48, 50-52, 54, 57, and 58 showed a maximum in the woelfling run which was done at the DFT/TPSS level. Among them only the sites 1, 2, 7, 12, 16, 18, 26, 32, 33, 43, 44, 48, and 50-52 had a peak higher than 0.0008 Hartree. Until now, we were able to optimize the transition state geometries for the sites 1, 2, 6, 7, 12, 18, 32, 33, 43, 44, 48, and 52. Therefore, here



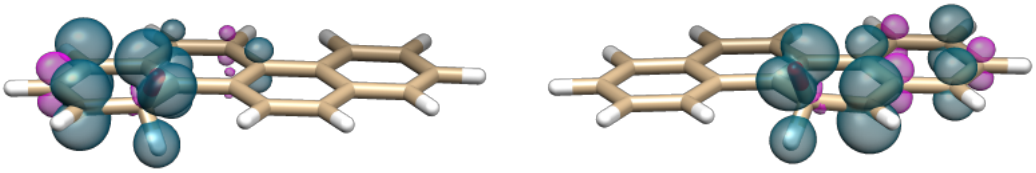
a) Fjord (50) b) Fjord* (56)

Figure 3.11: Comparison of the different fjord sites of benzo[c]phenanthrene. The numbering of the sites are according to the Figure 2.1



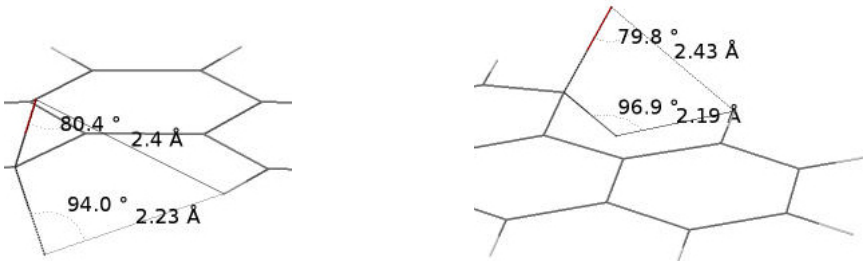
a) Bay (30) b) Bay (41)

Figure 3.12: Comparison of the different bay sites of benz[a]anthracene.



a) Bay (42) b) Bay (47)

Figure 3.13: Comparison of the different bay sites of chrysene.



a) Bay (42) b) Bay (47)

Figure 3.14: Comparison of the different bay sites of chrysene in terms of geometry.

we only report the activation barriers for these sites.(Table 3.16 and Figure 3.15)

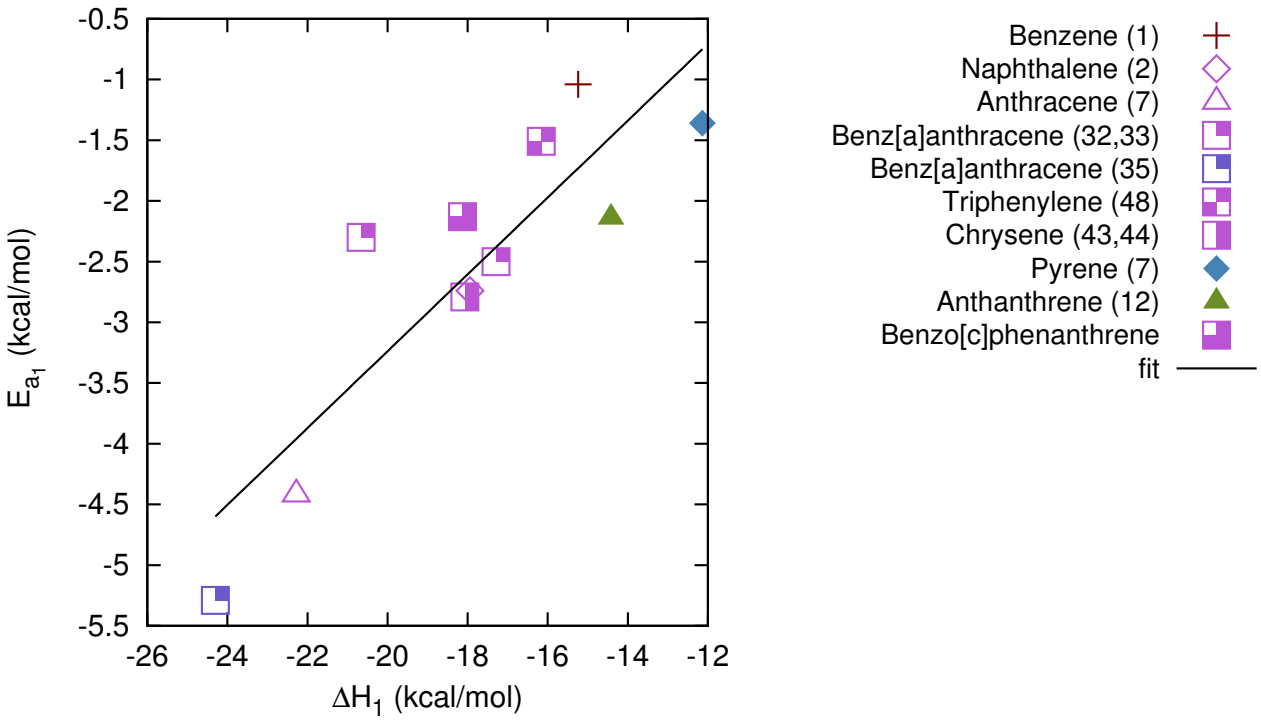


Figure 3.15: Ea_1 vs ΔH_1. The activation energies are taken relative to the energy of the separated reactants S1 and $O(^3P)$ as $Ea_1 = E_{TS1} - E_{S1} - E_{O(^3P)}$, not relative to the van der Waals minima.

The activation barriers show a linear correlation with the reaction energies (Figure 3.15). The fit is

$$Ea_1 = 0.32\Delta H_1 + 3.1\,[\text{kcal/mol}] \tag{3.4}$$

with $R^2 = 0.76$. That is, the Bell-Evans-Polanyi principle applies for this reaction. However, this data might not be enough to generalize it. The slope of the fit is less than 0.5. This indicates a reactant-like transition state, which is expected for an exothermic reaction with a barrier that is small compared to the reaction energy.

Table 3.16: Reaction energies and activation barriers of oxygen addition reaction. Units are in kcal/mol.

ID	ΔH_1	Ea_1	32	-17.3	-2.5
1	-15.2	-1.0	33	-20.7	-2.3
2	-17.9	-2.7	35	-24.3	-5.3
4	-22.3	-4.4	43	-18.1	-2.8
7	-12.1	-1.4	48	-16.2	-1.5
12	-14.4	-2.1	52	-18.1	-2.1

The activation energy of the reaction of naphthalene with an O-atom has been calculated to be 1.8±0.4 kcal/mol.[14] This is around 2.7 kcal/mol lower than the activation barrier of the reaction of benzene with an O-atom, which is around 4.5 kcal/mol [34, 27]. The difference between the activation barrier of site 2 of naphthalene and that of benzene is 1.7 kcal/mol. Even though the comparison is quantitatively poor, qualitatively we may say that one of the slow reactions for the combustion of naphthalene can be the O-atom addition reaction to the β-carbon.

3.1.4 Hydrogen Abstraction: Reaction Energies

The stabilization energies calculated for this reaction indicate that the orbital rearrangement is not the only important factor that determines the differences in the reaction energies. The fit is shown in Figure 3.17. The goodness of fit is $R^2 = 0.39$.

3.1.5 Hydrogen Abstraction: Activation Barriers

We could not yet optimize the transition state structures for site 30 and site 41. For the other sites, the activation barriers show a linear correlation with the reaction energies (Figure 3.15). The fit is

$$Ea_2 = 0.63\Delta H_2 + 6.7\,[\text{kcal/mol}] \tag{3.5}$$

with $R^2 = 0.68$.

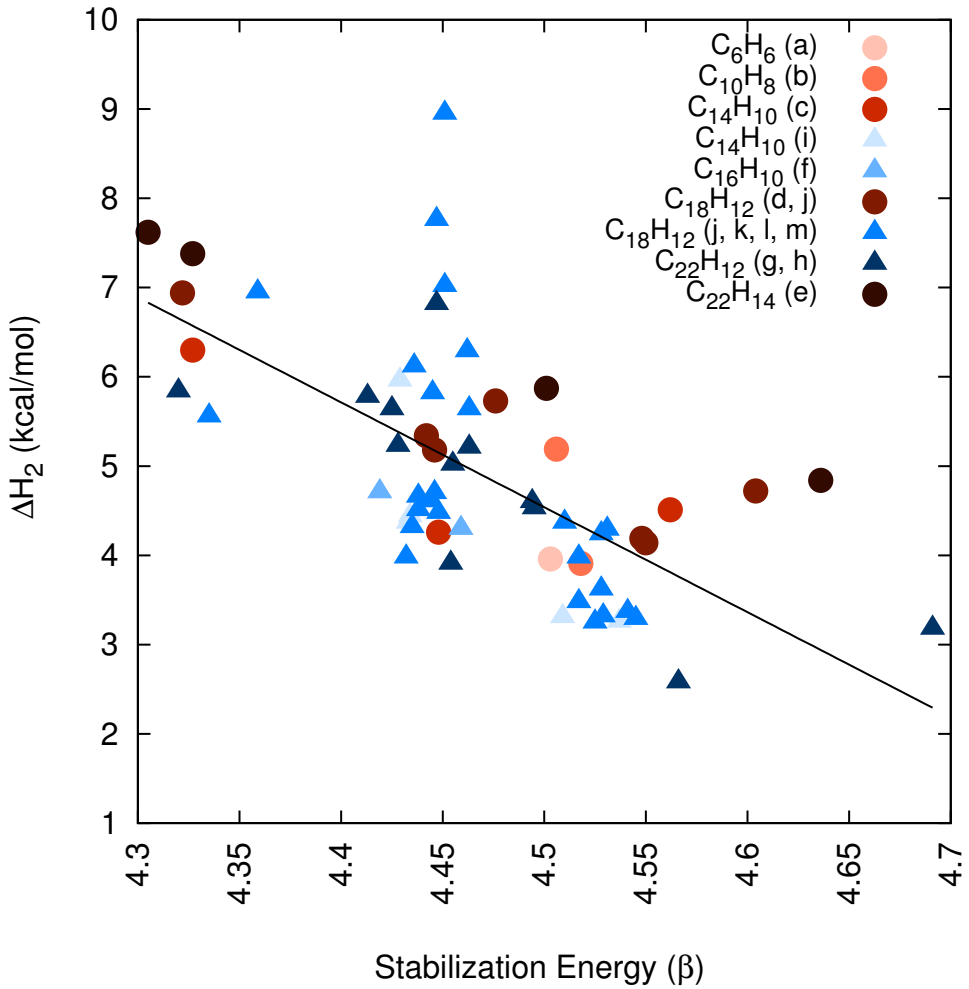


Figure 3.17: ΔH_2 as a function of stabilization energies.

The activation barrier calculated for benzene is 9.8 kcal/mol. This is lower than the value of 14.5 kcal/mol calculated by Nguyen et al.[33] and of 11.4 kcal/mol by Taatjes et al. [42] both of which were obtained at a higher level of theory than DFT/TPSSh-D3 level.

Comparing Figure 3.11 with Figure 3.20 for site 56, the reason that the activation barrier is higher than the BEP fit is probably because of the O—H interaction in the intermediate S2 structure. Before reaching the transition state, first this interaction should be weakened. The activation barrier at site 50 is also higher than the BEP fit, although not significantly. In this case, however, the reason is probably because of a transition state structure high in energy due to the H—H repulsion.

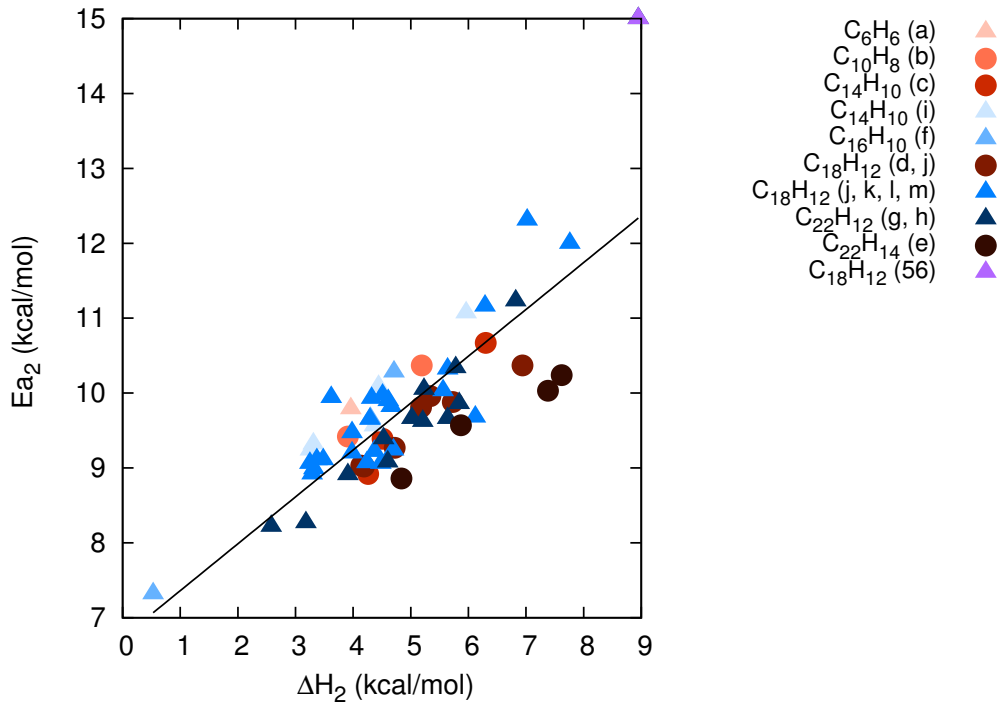
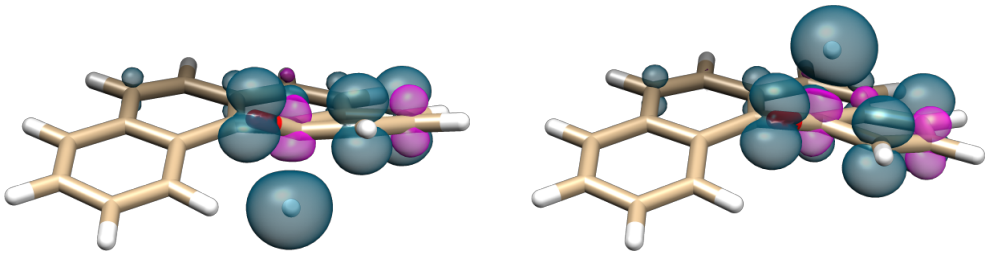


Figure 3.18: Ea_2 vs ΔH_2. Site 56 has a higher deviation than the fit as compared with the other data points.



a) Fjord (50) b) Fjord (56)

Figure 3.20: Comparison of the fjord sites of benzo[c]phenanthrene in TS2.

3.2 OH Abstraction Reaction of PAHs

The reaction can be formulated as

$$C_{2n}H_{n+a} + O(^3P) \longrightarrow \cdot C_{2n}H_{n+a-1} + \cdot OH \tag{3.6}$$

Table 3.19: Reaction energies and activation barriers of hydrogen abstraction reaction. Units are in kcal/mol.

ID	ΔH_2	Ea_2	22	2.6	8.2	43	3.3	9.0
1	4.0	9.8	23	5.2	10.1	44	3.3	9.1
2	3.9	9.4	24	5.0	9.7	45	4.6	9.9
3	5.2	10.4	25	5.2	9.6	46	4.0	9.2
4	4.5	9.4	26	3.9	8.9	47	5.6	10.3
5	4.3	8.9	27	4.7	9.3	48	4.4	9.2
6	6.3	10.7	28	5.7	9.9	49	7.8	12.0
7	0.5	7.3	29	6.9	10.4	50	7.0	12.3
8	4.7	10.3	30	5.8		51	3.5	9.1
9	4.3	9.7	31	3.3	8.9	52	4.2	9.1
10	4.5	9.4	32	3.4	9.1	53	4.7	9.8
11	5.6	9.7	33	4.3	9.7	54	6.1	9.7
12	3.2	8.3	34	4.7	9.2	55	4.3	9.9
13	5.8	10.3	35	4.5	9.1	56	9.0	15.0
14	5.8	9.9	36	5.6	10.0	57	4.0	9.5
15	4.6	9.1	37	5.3	10.0	58	3.6	9.9
16	3.3	9.2	38	4.2	9.0	59	4.5	10.0
17	6.0	11.1	39	4.1	9.0	60	4.8	8.9
18	3.3	9.3	40	5.2	9.8	61	5.9	9.6
19	4.4	10.1	41	7.0		62	7.4	10.0
20	4.4	9.6	42	6.3	11.2	63	7.6	10.2
21	6.8	11.2						

where $0 \leq a \leq 3$ for the set of PAHs considered. This reaction results in the breaking of the C-H bond. Figure 3.21 shows the intrinsic reaction coordinate of the OH abstraction reaction of benzene with $O(^3P)$. The singly occupied orbitals of the transition state structure, and the products $\cdot OH$ and $\cdot C_6H_5$ can be seen in Figure 3.22. The O-atom approaches to benzene on the molecular plane and then forms an O—H bond. Once the transition state is reached the OH radical is almost formed, as seen in Figure 3.21, and the geometry of products does not change significantly

from the TS to products. Therefore, the calculated activation barrier is close to the reaction energy.

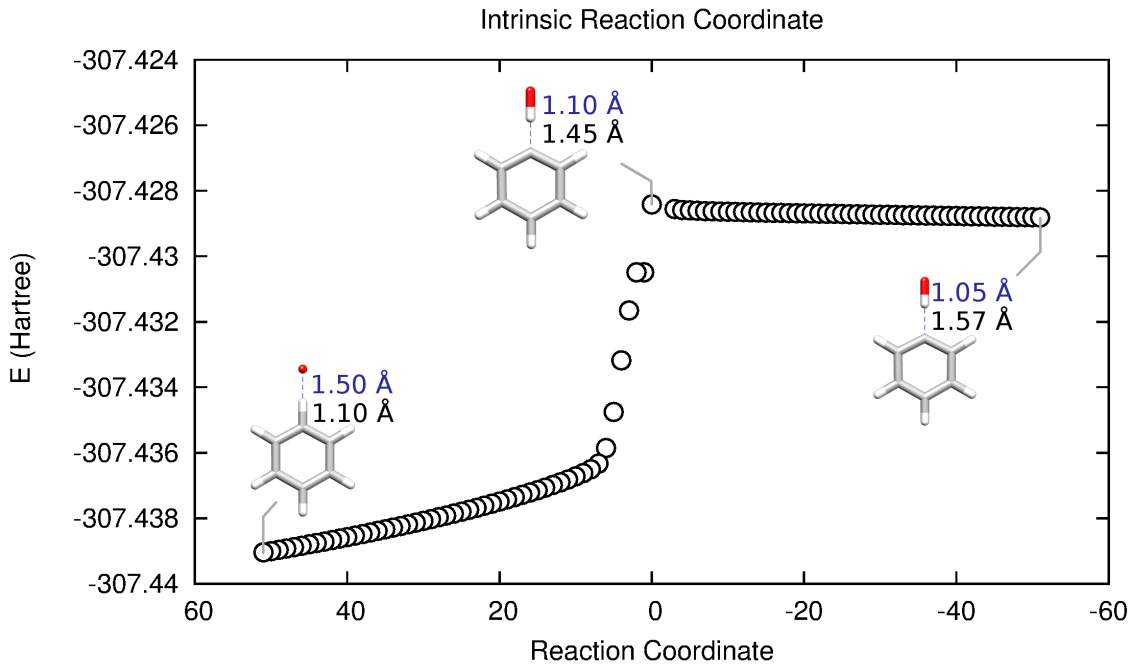


Figure 3.21: Intrinsic reaction coordinate of the OH abstraction reaction of benzene with O(^{3}P).

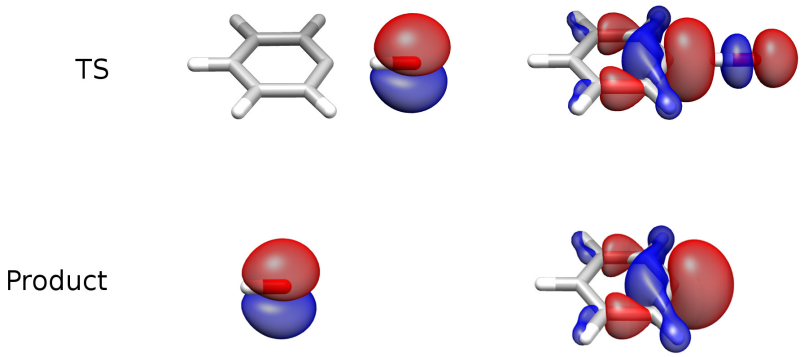


Figure 3.22: Singly occupied orbitals during the OH abstraction reaction of benzene with O(^{3}P).

Table 3.23: Reaction energies of OH abstraction reaction.

ID	ΔH_{OH}	11	6.67	22	5.61	33	5.70	44	5.65
1	5.41	12	5.91	23	6.42	34	5.44	45	5.72
2	5.63	13	6.85	24	6.01	35	5.46	46	5.56
3	5.89	14	7.00	25	6.00	36	6.09	47	3.76
4	5.71	15	6.40	26	6.14	37	5.70	48	6.55
5	5.96	16	4.48	27	5.33	38	5.42	49	3.90
6	6.39	17	5.80	28	5.57	39	5.44	50	-1.09
7	5.60	18	5.65	29	5.99	40	5.69	51	5.33
8	6.38	19	5.71	30	4.16	41	4.53	52	5.74
9	5.88	20	5.55	31	5.52	42	3.85	53	5.62
10	5.78	21		32	5.70	43	5.41	54	5.85
								55	5.67

Table 3.24: Activation energies for the OH abstraction reaction for the calculated sites.

ID	ΔH_{OH}	Ea_{OH}	20	5.55	4.78
1	5.41	5.29	26	6.14	5.21
2	5.63	5.30	35	5.46	4.25
7	5.60	5.07	42	3.85	4.34
9	5.88	4.78	45	5.72	4.79
16	4.48	4.66	46	5.56	4.35
17	5.80	5.11	49	3.90	5.94
19	5.71	4.94	52	5.74	5.60

The reaction energies are similar for each site. This is expected, because the reaction does not directly affect the π-system. Indeed, the π-system is only indirectly affected through the deformation of the geometry. The reaction at site 50 is exothermic as opposed to the reactions at other sites. This could be the effect of the change of geometry. The benz[a]anthracene molecule is helical in its ground state; however, upon OH abstraction reaction a product which is planar is formed, as

shown in Figure 3.25. This result will be verified once the transition state structure and the intrinsic reaction coordinate are found for site 50.

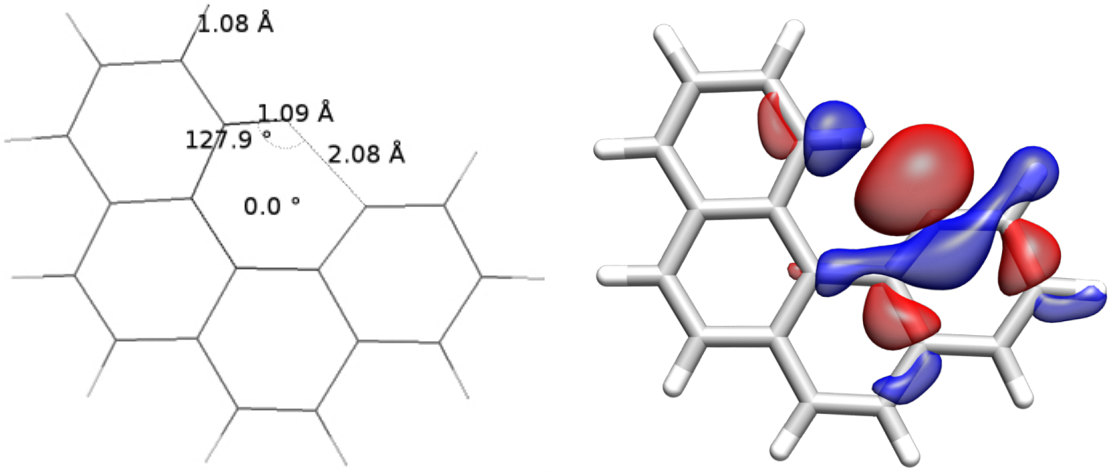


Figure 3.25: The geometry and the SOMO of the product formed after OH abstraction reaction at site 50.

The activation barrier of this step is calculated by Nguyen et al. as 11.6 kcal/mol for benzene with a reaction energy 12.2 kcal/mol.[33] DFT/TPSSh-D3 estimates lower reaction energies; however, it also estimates a lower activation barrier than the reaction energy. That is, the qualitative picture is the same as Nguyen for this reaction. Similar to benzene, in most of the structures, the activation barriers are smaller than the reaction energies, which implies that the activation barriers are from a van der Waals minimum of the products. The calculated activation barriers which are positive are for the bay regions of the chrysene (42) and triphenylene (49). However, this is not the case for the bay region of phenanthrene (17). In order to generalize activation barriers we need to find the transition state structures for all of the sites.

4 Conclusions and Summary

The reaction and activation energies obtained with DFT/TPSSh-D3 are for benzene lower than the literature values obtained at CBS-QB3 [33] and C3B3' level [42]. However, at a qualitative level the reaction pathways and structures agree well with the literature results.

The O-atom addition to the PAHs shows similarities on topologically similar sites. This is because the reaction energies directly correlate with the rearrangement of the orbitals, which is evidenced from the stabilization energy calculated by the HMO theory and the visualization of the unparied electron in the SOMO of the ring system. Further analysis evidenced that larger PAHs result in better delocalization, and hence, more exothermic O-atom addition reactions. Additionally, comparing analogous sites from linear and branched PAHs, the latter has less exothermic reactions. In particular, for the linear PAHs (acenes), the site on the inner ring has the most reactive C-H site within the molecule; and the reactivity towards O-atom addition increases with the increasing size of the acenes. Both of these effects are related with the delocalization of the orbitals. Finally, it was found that the calculated activation barriers of the reaction follow the Bell-Evans Polanyi (BEP) principle. The H abstraction reaction to form phenoxy-like radicals also follows the BEP principle. However, the site on the fjord region shows a significant deviation from this fit. We attributed this to the effect of hydrogen interaction within the molecule between O and fjord region hydrogens.

For the H radical abstraction reaction from the product of the O-atom addition, the orbital rearrangements are not the only factors that effect the reaction energies. The H abstraction reaction was also shown to follow the BEP principle. However, the site on the fjord region shows a significant deviation from this fit. This is attributed to the effect of hydrogen interaction within the molecule between O and fjord region

hydrogens.

The reaction energies of the OH abstraction reaction do not vary significantly. On the other hand, two of the activation barriers which exist both belong to the bay regions. The investigation of this reaction is not yet complete.

5 Outlook

In general, the H and OH radical abstraction reactions on the triplet surface might not be practical because of their relatively high activation barriers. Therefore, as a next step we plan to study the intersystem crossing of the S2 structures. To obtain experimentally comparable energies, we plan to calculate the energies using coupled cluster theory with single-, double-, and perturbative triple excitations (CCSD(T)) and pair natural orbitals. Then, we can investigate the analogous reactions proposed in the literature for the oxidation of benzene [33, 42], for the polycyclic aromatic hydrocarbons studied here.

Currently, the research group of Rochus Schmid studies the reaction network for the combustion of benzene using ReaxFF force field simulations in order to test the performance of ReaxFF. Simultaneously, we plan to use the proposed reactions and study them at the DFT/TPSSh-D3 and then at the CCSD(T) level. After a complete analysis is accomplished, we can build a benzene combustion model and compare the kinetics with the experimental values. If the reaction network model is validated, we can continue by building a model for larger systems.

For a more realistic picture, the bio-char samples from subproject A5 of the Oxyflame SFB/TRR 129 project can be analyzed using IR Spectroscopy, Raman spectroscopy, TEM measurements, and XRD analysis. Then, an improved char model can be suggested to perform ReaxFF simulations. The kinetic data obtained from these simulations can be compared with the reaction rates calculated from temperature programmed and isothermal oxidation measurements in the experimental subprojects.

The ultimate objective of the Oxyflame SFB/TRR 129 is to combine tools to characterize the structure of coal with a systematic approach to build kinetic

reaction networks to a predictive multiscale approach for modelling reactions thus to improve the design of reactors.

6 Acknowledgment

First of all, I would like to thank my family, and especially Filiz Özkırlı, for supporting my desire to discover the world of molecules. Without their support participating in this Masters program would not have been as easy. I am also very thankful to all of my friends who brought joy and inspiration to my daily life, and helped me to keep myself motivated whenever I felt in doubt.

I am very thankful to my supervisor, Christof Hättig, for his guidance and all the fruitful discussions. His wisdom on electronic structure theory catalyzed the analysis of the reactions studied in this thesis. I would also like to acknowledge my colleagues Sara K. Khani, Alireza M. Khah, and Chetana B. Viswanatha for expanding my understanding whenever my chemical knowledge was not enough to quickly grab a concept; and Marius Frank, for always being there whenever I was struggling with a technical problem.

Finally, I am thankful to the Chairman of the Board of Trustees, Gerd Hellmig from the Ruth and Gerth Massenberg Foundation, for partly funding the Deutschland Stipendium that I was awarded for the second year of my studies. I am also thankful to Jens Ränsch, Martin Muhler, and Christof Hättig for providing me a variety of student assistantship jobs during my studies. Their support removed most of the weight due to financial issues from my shoulders, and gave me a relieved mind to focus on my studies.

List of Figures

1.1 Simplified illustration of oxidation of coal. 3
1.2 Given bituminous coal model. 4
1.3 Reaction paths of O-atom addition reaction to benzene. 8

2.1 The sites for the linear and branched PAHs considered. 12
2.2 Molecular regions of polyarenes. 13
2.3 Some selected linear and branced polycyclic aromatic hydrocarbons and their HOMA values. 14
2.4 Correlation between resonance energy and angularity of the PAHs tetracene, benz[a]anthracene, chrysene, benzo[c]phenanthrene and triphenylene. 15

3.1 The reaction path of benzene for O(^{3}P) addition, following hydrogen radical abstraction reactions. 20
3.2 Singly occupied orbitals during the reaction of benzene with O(^{3}P). . 21
3.4 Enthalpy change of the oxygen addition reaction vs the stabilization energy classified according to the size of the molecules and fusion of the ring that the reaction proceeds. 23
3.6 SOMOs of the PAHs studied for the structure S2. 25
3.7 Comparison of the reaction energies for different sites of linear PAHs. 26
3.8 Reaction energies, ΔH_1, and the activation barriers, (Ea_1), for the angularly fused PAHs. 28
3.9 Classification of the quartet sites. 29
3.10 Reaction energy vs stabilization energy. 30
3.11 Comparison of the different fjord sites of benzo[c]phenanthrene. . . . 31
3.12 Comparison of the different bay sites of benz[a]anthracene. 31
3.13 Comparison of the different bay sites of chrysene. 31

3.14 Comparison of the different bay sites of chrysene in terms of geometry. 31
3.15 Ea_1 vs ΔH_1. 32
3.17 ΔH_2 as a function of stabilization energies. 34
3.18 Ea_2 vs ΔH_2. 35
3.20 Comparison of the fjord sites of benzo[c]phenanthrene in TS2. 35
3.21 Intrinsic reaction coordinate of the OH abstraction reaction of benzene with $O(^3P)$. 37
3.22 Singly occupied orbitals during the OH abstraction reaction of benzene with $O(^3P)$. 37
3.25 The geometry and the SOMO of the product formed after OH abstraction reaction at site 50. 39

A.1 SOMO of C_5H_5 54

List of Tables

3.3 The change in the C-H bond length from the reactant S1 to the intermediate S2 and to the transition state TS1. 22

3.5 The stabilization energies, the ΔH_1 values calculated using DFT, the ΔH_1 values calculated from the stabilization energy fit, and $\Delta = \Delta H_1$ -ΔH_1(fit). 24

3.16 Reaction energies and activation barriers of oxygen addition reaction. 33

3.19 Reaction energies and activation barriers of hydrogen abstraction reaction. 36

3.23 Reaction energies of OH abstraction reaction. 38

3.24 Activation energies for the OH abstraction reaction for the calculated sites. 38

A.2 The energies of the S1 structures. 55

A.3 The energies of the S2 structures. 56

A.4 The energies of the S3 structures. 57

A.5 The energies of the TS1 structures. 58

A.6 The energies of the TS2 structures. 59

A.7 The energies of the products analogous to the phenyl radical. 60

A.8 The energies of the TS-OH structures. 61

Bibliography

[1] TURBOMOLE V7.1 2016, a development of University of Karlsruhe and Forschungszentrum Karlsruhe GmbH, 1989-2007, TURBOMOLE GmbH, since 2007; available from `http://www.turbomole.com`.

[2] S. W. Benson, F. R. Cruickshank, D. M. Golden, G. R. Haugen, H. E. O'Neal, A. S. Rodgers, R. Shaw, and R. Walsh. Additivity rules for the estimation of thermochemical properties. *Chemical Reviews*, 69(3):279–324, 1969.

[3] S. Bhoi, T. Banerjee, and K. Mohanty. Molecular dynamic simulation of spontaneous combustion and pyrolysis of brown coal using reaxff. *Fuel*, 136:326 – 333, 2014.

[4] K. Brezinsky. The high-temperature oxidation of aromatic hydrocarbons. *Progress in Energy and Combustion Science*, 12(1):1 – 24, 1986.

[5] F. Castro-Marcano, A. M. Kamat, M. F. Russo, A. C. van Duin, and J. P. Mathews. Combustion of an Illinois No. 6 coal char simulated using an atomistic char representation and the ReaxFF reactive force field. *Combustion and Flame*, 159(3):1272 – 1285, 2012.

[6] L. Chen, S. Z. Yong, and A. F. Ghoniem. Oxy-fuel combustion of pulverized coal: Characterization, fundamentals, stabilization and CFD modeling. *Progress in Energy and Combustion Science*, 38(2):156 – 214, 2012.

[7] E. Clar. Hexacen, ein grüner, einfacher Kohlenwasserstoff (Aromatische Kohlenwasserstoffe, XXIV. mitteil.). *Berichte der deutschen chemischen Gesellschaft (A and B Series)*, 72(10):1817–1821, 1939.

[8] W. E, W. Ren, and E. Vanden-Eijnden. String method for the study of rare events. *Phys. Rev. B*, 66:052301, Aug 2002.

[9] S. Ehrlich, H. F. Bettinger, and S. Grimme. Dispersion-driven conformational isomerism in σ-bonded dimers of larger acenes. *Angewandte Chemie International Edition*, 52(41):10892–10895, 2013.

[10] K. Eichkorn, F. Weigend, O. Treutler, and R. Ahlrichs. Auxiliary basis sets for main row atoms and transition metals and their use to approximate Coulomb potentials. *Theoretical Chemistry Accounts*, 97(1):119–124, Oct 1997.

[11] J. L. Emdee, K. Brezinsky, and I. Glassman. A kinetic model for the oxidation of toluene near 1200 K. *The Journal of Physical Chemistry*, 96(5):2151–2161, 1992.

[12] A. C. Ferrari. Raman spectroscopy of graphene and graphite: Disorder, electron–phonon coupling, doping and nonadiabatic effects. *Solid State Communications*, 143(1):47 – 57, 2007. Exploring graphene.

[13] A. C. Ferrari and D. M. Basko. Raman spectroscopy as a versatile tool for studying the properties of graphene. *Nature Nanotechnology*, 8(4):235–246, 2013.

[14] H. Frerichs, R. Koch, M. Tappe, and H. G. Wagner. Investigation of the reaction of naphthalene with O(3P) in the gas phase. *Zeitschrift für Naturforschung A*, 44a:1119–1121, 1989.

[15] K. Fukui. The path of chemical reactions - the irc approach. *Accounts of Chemical Research*, 14(12):363–368, 1981.

[16] P. H. Given. Structure of bituminous coals: Evidence from distribution of hydrogen. *Nature*, 184(4691):980–981, 1959.

[17] S. Grimme, J. Antony, S. Ehrlich, and H. Krieg. A consistent and accurate ab initio parametrization of density functional dispersion correction (DFT-D) for the 94 elements H-Pu. *The Journal of Chemical Physics*, 132(15):154104, 2010.

[18] T. A. Halgren and W. N. Lipscomb. The synchronous-transit method for determining reaction pathways and locating molecular transition states. *Chemical Physics Letters*, 49(2):225 – 232, 1977.

[19] R. Harvey. *Polycyclic Aromatic Hydrocarbons: Chemistry and Carcinogenicity.* Cambridge Monographs on Cancer Research. Cambridge University Press, 1991.

[20] R. G. Harvey. *Polycyclic Aromatic Hydrocarbons.* Wiley-VCH, New York, NY, U.S.A., 1997.

[21] T. Helgaker. Transition-state optimizations by trust-region image minimization. *Chemical Physics Letters*, 182(5):503 – 510, 1991.

[22] G. Henkelman and H. Jónsson. A dimer method for finding saddle points on high dimensional potential surfaces using only first derivatives. *The Journal of Chemical Physics*, 111(15):7010–7022, 1999.

[23] G. Henkelman and H. Jónsson. Improved tangent estimate in the nudged elastic band method for finding minimum energy paths and saddle points. *The Journal of Chemical Physics*, 113(22):9978–9985, 2000.

[24] G. Henkelman, B. P. Uberuaga, and H. Jónsson. A climbing image nudged elastic band method for finding saddle points and minimum energy paths. *The Journal of Chemical Physics*, 113(22):9901–9904, 2000.

[25] A. Heyden, A. T. Bell, and F. J. Keil. Efficient methods for finding transition states in chemical reactions: Comparison of improved dimer method and partitioned rational function optimization method. *The Journal of Chemical Physics*, 123(22):224101, 2005.

[26] F. Jensen. *Introduction to Computational Chemistry.* Wiley, 2007.

[27] T. Ko, G. Y. Adusei, and A. Fontijn. Kinetics of the atomic oxygen(^{3}P) + benzene reaction over a wide temperature range. *The Journal of Physical Chemistry*, 95(22):8745–8748, 1991.

[28] J. Kruszewski and T. Krygowski. Definition of aromaticity basing on the harmonic oscillator model. *Tetrahedron Letters*, 13(36):3839 – 3842, 1972.

[29] N. M. Laurendeau. Heterogeneous kinetics of coal char gasification and combustion. *Progress in Energy and Combustion Science*, 4(4):221 – 270, 1978.

[30] H. Liu. Combustion of coal chars in O_2/CO_2 and O_2/N_2 mixtures: a comparative study with non-isothermal thermogravimetric analyzer (TGA) tests. *Energy & Fuels*, 23(9):4278–4285, 2009.

[31] L. Lu, C. Kong, V. Sahajwalla, and D. Harris. Char structural ordering during pyrolysis and combustion and its influence on char reactivity. *Fuel*, 81(9):1215 – 1225, 2002.

[32] J. P. Mathews and A. L. Chaffee. The molecular representations of coal - A review. *Fuel*, 96:1 – 14, 2012.

[33] T. L. Nguyen, J. Peeters, and L. Vereecken. Theoretical reinvestigation of the $O(^3P) + C_6H_6$ reaction. *The Journal of Physical Chemistry A*, 111(19):3836–3849, 2007. PMID: 17253662.

[34] J. M. Nicovich, C. A. Gump, and A. R. Ravishankara. Rates of reactions of atomic oxygen(^3P) with benzene and toluene. *The Journal of Physical Chemistry*, 86(9):1684–1690, 1982.

[35] P. Plessow. Reaction path optimization without NEB springs or interpolation algorithms. *Journal of Chemical Theory and Computation*, 9(3):1305–1310, 2013. PMID: 26587592.

[36] A. Pullman and B. Pullman. Electronic structure and carcinogenic activity of aromatic molecules new developments. *Advances in Cancer Research*, 3:117 – 169, 1955.

[37] P. v. R. Schleyer, M. Manoharan, H. Jiao, and F. Stahl. The acenes: is there a relationship between aromatic stabilization and reactivity? *Organic Letters*, 3(23):3643–3646, 2001. PMID: 11700102.

[38] C. Sheng. Char structure characterised by Raman spectroscopy and its correlations with combustion reactivity. *Fuel*, 86(15):2316 – 2324, 2007.

[39] I. Smith. The combustion rates of coal chars: A review. *Symposium (International) on Combustion*, 19(1):1045 – 1065, 1982. Nineteenth Symposium (International) on Combustion.

[40] M. W. Smith, I. Dallmeyer, T. J. Johnson, C. S. Brauer, J.-S. McEwen, J. F. Espinal, and M. Garcia-Perez. Structural analysis of char by Raman spectroscopy: Improving band assignments through computational calculations from first principles. *Carbon*, 100:678 – 692, 2016.

[41] V. N. Staroverov, G. E. Scuseria, J. Tao, and J. P. Perdew. Comparative assessment of a new nonempirical density functional: Molecules and hydrogen-bonded complexes. *The Journal of Chemical Physics*, 119(23):12129–12137, 2003.

[42] C. A. Taatjes, D. L. Osborn, T. M. Selby, G. Meloni, A. J. Trevitt, E. Epifanovsky, A. I. Krylov, B. Sirjean, E. Dames, and H. Wang. Products of the benzene + O(^{3}P) reaction. *The Journal of Physical Chemistry A*, 114(9):3355–3370, 2010. PMID: 20099861.

[43] Y. Tan, E. Croiset, M. A. Douglas, and K. V. Thambimuthu. Combustion characteristics of coal in a mixture of oxygen and recycled flue gas. *Fuel*, 85(4):507 – 512, 2006.

[44] J. Tao, J. P. Perdew, V. N. Staroverov, and G. E. Scuseria. Climbing the density functional ladder: Nonemrical meta–generalized gradient approximation designed for molecules and solids. *Phys. Rev. Lett.*, 91:146401, Sep 2003.

[45] K. P. Vijayalakshmi and C. H. Suresh. Theoretical studies on the carcinogenicity of polycyclic aromatic hydrocarbons. *Journal of Computational Chemistry*, 29(11):1808–1817, 2008.

[46] G. Várhegyi, P. Szabó, E. Jakab, F. Till, and J.-R. Richard. Mathematical modeling of char reactivity in Ar-O_2 and CO_2-O_2 mixtures. *Energy & Fuels*, 10(6):1208–1214, 1996.

[47] G. Várhegyi and F. Till. Comparison of temperature-programmed char combustion in CO_2-O_2 and Ar-O_2 mixtures at elevated pressure. *Energy & Fuels*, 13(2):539–540, 1999.

[48] H. Wang, B. Z. Dlugogorski, and E. M. Kennedy. Coal oxidation at low temperatures: oxygen consumption, oxidation products, reaction mechanism and

kinetic modelling. *Progress in Energy and Combustion Science*, 29(6):487 – 513, 2003.

[49] F. Weigend. Accurate Coulomb-fitting basis sets for H to Rn. *Phys. Chem. Chem. Phys.*, 8:1057–1065, 2006.

[50] S. S. Zade, N. Zamoshchik, A. R. Reddy, G. Fridman-Marueli, D. Sheberla, and M. Bendikov. Products and mechanism of acene dimerization. a computational study. *Journal of the American Chemical Society*, 133(28):10803–10816, 2011. PMID: 21710966.

[51] E. Zadok, B. Sialom, and Y. Mazur. Oxygen atoms produced by microwave discharge: Reaction with arenes. *Angewandte Chemie International Edition in English*, 19(12):1004–1005, 1980.

[52] M. Zander. In A. Bjorseth, editor, *Handbook of Polycyclic Aromatic Hydrocarbons*, pages 1–20. Marcel Dekker, New York, NY, U.S.A., 1983.

A Appendix

A.1 Sample Stabilization Energy Calculation

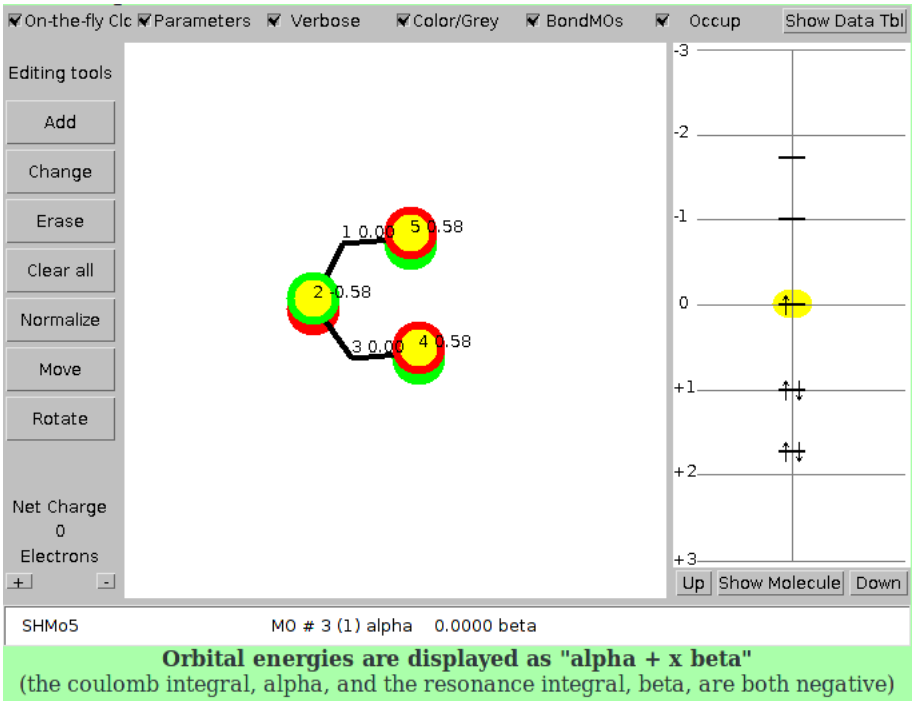


Figure A.1: SOMO of C_5H_5

Sample Calculation of Stabilization Energy:

Total energy of C_6H_6 = 6 α+ **8** β

Total energy of C_5H_5 = 5 α+ **5.464** β

Stabilization energy = 5.464 β - 8 β = -2.536 β

A.2 Energies of the Optimized Structures

A.2.1 Oxygen Addition and Hydrogen Abstraction Reaction

Table A.2: The energies of the S1 structures using TPSSh functional TZVP basis set and Grimme D3 correction in Hartree.

Molecule	**Formula**	**E+ZPE**	**ZPE**
Benzene	C_6H_6	-232.2458641	0.0999461
Naphtalene	$C_{10}H_8$	-385.9052117	0.1461926
Anthracene	$C_{14}H_{10}$	-539.5590464	0.1921374
Phenanthrene	$C_{14}H_{10}$	-539.5676584	0.1922026
Pyrene	$C_{16}H_{10}$	-615.8186149	0.2046137
Tetracene	$C_{18}H_{12}$	-693.2108602	0.2377771
Benzo[c]phenanthrene	$C_{18}H_{12}$	-693.2181005	0.2394228
Benz[a]anthracene	$C_{18}H_{12}$	-693.2237136	0.2384996
Chrysene	$C_{18}H_{12}$	-693.2278411	0.2382342
Triphenylene	$C_{18}H_{12}$	-693.2297005	0.2362373
Anthanthrene	$C_{22}H_{12}$	-845.7258224	0.2613539
Benzo[ghi]perylene	$C_{22}H_{12}$	-845.7322602	0.2643857
Pentacene	$C_{22}H_{14}$	-846.8615183	0.2834722

Table A.3: The energies of the S2 structures using TPSSh functional TZVP basis set and Grimme D3 correction in Hartree.

using TPSSh functional TZVP basis set and Grimme D3 correction

ID	**E+ZPE**	**ZPE**	32	-768.3493813	0.2377830
1	-307.3682649	0.0991248	33	-768.3547410	0.2378554
2	-461.0319093	0.1455928	34	-768.3618246	0.2383755
3	-461.0400603	0.1458314	35	-768.3605435	0.2384761
4	-614.6926667	0.1915411	36	-768.3704318	0.2390852
5	-614.6981243	0.1932956	37	-768.3628465	0.2381550
6	-614.7104949	0.1928724	38	-768.3546256	0.2379609
7	-690.9360774	0.2049913	39	-768.3552271	0.2379327
8	-690.9586634	0.2043945	40	-768.3626064	0.2382540
9	-690.9540461	0.2042980	41	-768.3687503	0.2390080
10	-920.8637370	0.2617716	42	-768.3602476	0.2379750
11	-920.8733784	0.2624604	43	-768.3547535	0.2376703
12	-920.8469178	0.2613145	44	-768.3528240	0.2376253
13	-920.8739694	0.2627226	45	-768.3607385	0.2377452
14	-920.8787854	0.2636414	46	-768.3629590	0.2384287
15	-920.8636820	0.2622364	47	-768.3589626	0.2386437
16	-614.6942566	0.1917259	48	-768.3535560	0.2369274
17	-614.6986774	0.1920769	49	-768.3581635	0.2377310
18	-614.6921619	0.1915947	50	-768.3470904	0.2393648
19	-614.6995308	0.1917520	51	-768.3453049	0.2389320
20	-614.7015924	0.1920008	52	-768.3450990	0.2387324
21	-920.8710177	0.2644832	53	-768.3513831	0.2388793
22	-920.8526628	0.2634535	54	-768.3553092	0.2391416
23	-920.8718622	0.2641410	55	-768.3506824	0.2391328
24	-920.8691961	0.2631820	56	-768.3501723	0.2404222
25	-920.8671113	0.2628864	57	-768.3461190	0.2389411
26	-920.8625452	0.2634090	58	-768.3440928	0.2389583
27	-768.3498015	0.2371258	59	-768.3511329	0.2389777
28	-768.3557811	0.2374725	60	-922.0046020	0.2826144
29	-768.3713220	0.2388216	61	-922.0092757	0.2829832
30	-768.3540959	0.2383591	62	-922.0276449	0.2845275
31	-768.3513001	0.2379469	63	-922.0323116	0.2848628

Table A.4: The energies of the S3 structures using TPSSh functional TZVP basis set and Grimme D3 correction in Hartree.

ID	**E+ZPE**	**ZPE**	32	-767.8441493	0.2286149
1	-306.8620939	0.0905219	33	-767.8480543	0.2292721
2	-460.5258179	0.1365961	34	-767.8544736	0.2293931
3	-460.5319286	0.1372795	35	-767.8535500	0.2295261
4	-614.1856305	0.1824056	36	-767.8617109	0.2301159
5	-614.1914826	0.1832586	37	-767.8544828	0.2295326
6	-614.2006066	0.1839196	38	-767.8480899	0.2287694
7	-690.4353809	0.1940865	39	-767.8487751	0.2287578
8	-690.4513053	0.1951948	40	-767.8544952	0.2296817
9	-690.4473460	0.1952175	41	-767.8578146	0.2300864
10	-920.3566694	0.2530800	42	-767.8503757	0.2290633
11	-920.3645422	0.2534757	43	-767.8496059	0.2284819
12	-920.3419921	0.2538561	44	-767.8477879	0.2283442
13	-920.3649072	0.2536422	45	-767.8535382	0.2291197
14	-920.3696304	0.2546884	46	-767.8567599	0.2291799
15	-920.3564947	0.2536283	47	-767.8501249	0.2288582
16	-614.1892101	0.1824489	48	-767.8467429	0.2297390
17	-614.1893201	0.1830087	49	-767.8459495	0.2298201
18	-614.1870341	0.1824130	50	-767.8360520	0.2304208
19	-614.1925938	0.1830237	51	-767.8399089	0.2302646
20	-614.1947788	0.1830712	52	-767.8384827	0.2302531
21	-920.3602964	0.2562962	53	-767.8440979	0.2305913
22	-920.3487040	0.2557319	54	-767.8457066	0.2308321
23	-920.3636800	0.2561172	55	-767.8439415	0.2306055
24	-920.3613467	0.2559994	56	-767.8360541	0.2304186
25	-920.3589588	0.2559581	57	-767.8399219	0.2302497
26	-920.3564520	0.2559997	58	-767.8384731	0.2302610
27	-767.8424251	0.2278526	59	-767.8440949	0.2305859
28	-767.8467897	0.2289701	60	-921.4970328	0.2733019
29	-767.8604084	0.2296850	61	-921.5000695	0.2745676
30	-767.8449631	0.2292870	62	-921.5160316	0.2754069
31	-767.8461972	0.2288669	63	-921.5203159	0.2754846

Table A.5: The energies of the TS1 structures using TPSSh functional TZVP basis set and Grimme D3 correction in Hartree.

ID	**E+ZPE**	**ZPE**
1	-307.34562820	0.09996470
2	-461.00768770	0.14664490
4	-614.66419220	0.19264050
7	-690.91888420	0.20532150
12	-920.82734080	0.26257610
32	-768.32580400	0.23851540
33	-768.32548950	0.24035980
35	-768.33025880	0.23881940
43	-768.33039120	0.23854440
48	-768.33021130	0.23776990
52	-768.31961190	0.23975410
58	-768.32118820	0.23992130

Table A.6: The energies of the TS2 structures using TPSSh functional TZVP basis set and Grimme D3 correction in Hartree.

ID	**E+ZPE**	**ZPE**	32	-768.3348584	0.2313392
1	-307.3526686	0.0932890	33	-768.3393593	0.2317087
2	-461.0168979	0.1394299	34	-768.3471073	0.2318037
3	-461.0235360	0.1399943	35	-768.3461094	0.2318769
4	-614.6777007	0.1849975	36	-768.3544417	0.2322732
5	-614.6839108	0.1855935	37	-768.3469792	0.2315544
6	-614.6934881	0.1863280	38	-768.3402582	0.2309475
7	-690.9244131	0.1976665	39	-768.3408384	0.2309947
8	-690.9422816	0.1982744	40	-768.3469679	0.2317252
9	-690.9386463	0.1985675	41	-768.3600038	0.2309792
10	-920.8487772	0.2558332	42	-768.3424621	0.2316268
11	-920.8579776	0.2549524	43	-768.3404257	0.2311913
12	-920.8337458	0.2554816	44	-768.3383855	0.2313487
13	-920.8574992	0.2558789	45	-768.3449570	0.2317659
14	-920.8630728	0.2565349	46	-768.3483009	0.2321383
15	-920.8492043	0.2558582	47	-768.3425115	0.2317603
16	-614.6795335	0.1855866	48	-768.3388566	0.2310485
17	-614.6810333	0.1859235	49	-768.3390427	0.2323829
18	-614.6773150	0.1856336	50	-768.3274721	0.2323014
19	-614.6834593	0.1861097	51	-768.3307866	0.2328320
20	-614.6863500	0.1862218	52	-768.3306383	0.2327023
21	-920.8531145	0.2583337	53	-768.3357333	0.2330295
22	-920.8395571	0.2575302	54	-768.3398761	0.2329396
23	-920.8558398	0.2580073	55	-768.3348605	0.2331469
24	-920.8538008	0.2577989	56	-768.3262647	0.2326787
25	-920.8517755	0.2577385	57	-768.3310276	0.2327192
26	-920.8483479	0.2574430	58	-768.3282456	0.2328292
27	-768.3350298	0.2303147	59	-768.3352415	0.2329784
28	-768.3400322	0.2309728	60	-921.9904840	0.2752461
29	-768.3547907	0.2316524	61	-921.9940301	0.2763401
30			62	-922.0116667	0.2771261
31	-768.3370784	0.2312737	63	-922.0159853	0.2773562

A.2.2 OH Abstraction Reaction

Table A.7: The energies of the products analogous to the phenyl radical using TPSSh functional TZVP basis set and Grimme D3 correction in Hartree.

ID	**E+ZPE**	**ZPE**	28	-692.5368557	0.2247312
1	-231.5721166	0.0859133	29	-692.5361882	0.2250012
2	-385.2311123	0.1317799	30	-692.5519587	0.2256127
3	-385.2307045	0.1319949	31	-692.5497851	0.2253702
4	-538.8848135	0.1773027	32	-692.5495087	0.2252578
5	-538.8844144	0.1775198	33	-692.5495070	0.2254527
6	-538.8837444	0.1777760	34	-692.5499128	0.2252510
7	-615.1445681	0.1894433	35	-692.5498787	0.2253070
8	-615.1433241	0.1898308	36	-692.5488790	0.2257165
9	-615.1441215	0.1896975	37	-692.5494976	0.2254333
10	-845.0514828	0.2487507	38	-692.5499463	0.2252317
11	-845.0500721	0.2493843	39	-692.5499228	0.2252314
12	-845.0512825	0.2490962	40	-692.5495203	0.2254900
13	-845.0497877	0.2464737	41	-692.5513715	0.2258438
14	-845.0495446	0.2497880	42	-692.5565852	0.2253238
15	-845.0504941	0.2497003	43	-692.5540940	0.2250400
16	-538.8953918	0.1777198	44	-692.5537131	0.2249346
17	-538.8932931	0.1774871	45	-692.5535954	0.2251871
18	-538.8935330	0.1789496	46	-692.5538581	0.2251234
19	-538.8934254	0.1792061	47	-692.5567173	0.2252287
20	-538.8936910	0.1790561	48	-692.5541309	0.2244985
21			49	-692.5583620	0.2239213
22	-845.0581889	0.2516616	50	-692.5547060	0.2249803
23	-845.0569054	0.2518113	51	-692.5444745	0.2263023
24	-845.0575545	0.2517824	52	-692.5438343	0.2263166
25	-845.0575717	0.2518133	53	-692.5440176	0.2264918
26	-845.0573414	0.2518551	54	-692.5436539	0.2264511
27	-692.5372398	0.2244810	55	-692.5439445	0.2264302

Table A.8: The energies of the TS-OH structures using TPSSh functional TZVP basis set and Grimme D3 correction in Hartree.

ID	**E+ZPE**	**ZPE**
1	-307.3355414	0.0928748
2	-460.9948785	0.1390996
7	-690.9086404	0.1972211
9	-690.9091072	0.1976449
16	-614.6583478	0.1851998
17	-614.6576180	0.1849859
19	-614.6578929	0.1853858
20	-614.6581506	0.1852754
26	-920.8220746	0.2578562
35	-768.3150512	0.2309074
42	-768.3190273	0.2308326
45	-768.3183119	0.2311302
46	-768.3190209	0.2308292
49	-768.3183363	0.2308691
52	-768.3072921	0.2325339